JCB Journal of Cell Biology

ARTICLE

Ecm29-mediated proteasomal distribution modulates excitatory GABA responses in the developing brain

Min Lee, Yen-Chen Liu, Chen Chen, Chi-Huan Lu, Shao-Tzu Lu, Tzyy-Nan Huang, Meng-Tsung Hsu, Yi-Ping Hsueh, and Pei-Lin Cheng

Neuronal GABAergic responses switch from excitatory to inhibitory at an early postnatal period in rodents. The timing of this switch is controlled by intracellular Cl^- concentrations, but factors determining local levels of cation-chloride cotransporters remain elusive. Here, we report that local abundance of the chloride importer NKCC1 and timely emergence of GABAergic inhibition are modulated by proteasome distribution, which is mediated through interactions of proteasomes with the adaptor Ecm29 and the axon initial segment (AIS) scaffold protein ankyrin G. Mechanistically, both the Ecm29 N-terminal domain and an intact AIS structure are required for transport and tethering of proteasomes in the AIS region. In mice, Ecm29 knockout (KO) in neurons increases the density of NKCC1 protein in the AIS region, a change that positively correlates with a delay in the GABAergic response switch. Phenotypically, Ecm29 KO mice showed increased firing frequency of action potentials at early postnatal ages and were hypersusceptible to chemically induced convulsive seizures. Finally, Ecm29 KO neurons exhibited accelerated AIS developmental positioning, reflecting a perturbed AIS morphological plastic response to hyperexcitability arising from proteasome inhibition, a phenotype rescued by ectopic Ecm29 expression or NKCC1 inhibition. Together, our findings support the idea that neuronal maturation requires regulation of proteasomal distribution controlled by Ecm29.

Introduction

Local protein turnover reduces cellular stress caused by aberrant protein accumulation, which can promote inadequate responses to external physiological stimuli. The 26S proteasome complex is required for protein degradation, which maintains protein homeostasis to meet multiple needs of functionally independent cellular compartments, especially in cells with highly polarized morphologies (Terenzio et al., 2017). Mature neurons are polarized into axonal and somatodendritic compartments segregated via a specialized membrane domain, the axon initial segment (AIS; Grubb et al., 2011; Rasband, 2010). The AIS serves as a protein transport and membrane diffusion checkpoint and relies on the highly organized cytoskeletal adaptor protein ankyrin G (AnkG), which accumulates in the AIS via interactions with other scaffold proteins (Kole and Stuart, 2012; Leterrier, 2018). Whether and how proteasome complexes and AIS structures function together to control neuronal maturation is not known.

Prior to AIS formation in newly differentiated hippocampal neurons, a long-range transport mechanism reportedly selectively controls proteasome abundance in nascent axons (Hsu et al., 2015; Otero et al., 2014). Directional proteasome transport in neurons requires association of the proteasome adaptor protein Ecm29 with microtubule-associated motor proteins kinesin family member 5B (KIF5B) and/or dynein (Gorbea et al., 2004, 2010; Hsu et al., 2015; Otero et al., 2014). As a major proteasome adaptor/scaffold and chaperone (Kajava et al., 2004; Leggett et al., 2002; Wani et al., 2016), Ecm29 confers functions in both proteasome particle assembly/disassembly and proteasome mobility/localization via direct proteasome interactions under different cell contexts (De La Mota-Peynado et al., 2013; Lee et al., 2011; Lehmann et al., 2010; Panasenko and Collart, 2011; Wang et al., 2017b; Wani et al., 2016). It is likely that Ecm29-associated proteasomal activity and distribution change as neurons mature morphologically and functionally. As such, cytoplasmic 26S proteasome particles targeting different subcellular compartments may require diverse Ecm29 associations with different sets of adaptors, depending on local molecular and structural properties (Gorbea et al., 2010; Tai et al., 2010). However, whether and how Ecm29 controls proteasome targeting or retention to newly emerged subcellular structures, such as the AIS membrane or synapses, is unclear.

Institute of Molecular Biology, Academia Sinica, Taipei, Taiwan.

Correspondence to Pei-Lin Cheng: plcheng@imb.sinica.edu.tw.

As a structure, the AIS initially appears at the proximal end of a growing axon within the first few postnatal days (P; P1 to P2 for rat cortical neurons in vivo [Galiano et al., 2012]) or in 2–7 d in vitro (DIV; in rat cortical/hippocampal cultures [Yang et al., 2007]) before young neurons undergo several stages of structural remodeling concurrent with emergence of neuronal activity (Yang et al., 2007). Precisely when the AIS is initially optimized to modulate synaptic input and output in afferent rodent cells remains unclear. Notably, apart from the AIS serving as the initiation site for action potentials (APs) in mature neurons, AIS formation is closely followed by an excitation-to-inhibition transition in the case of γ-aminobutyric acid (GABA)-ergic responses. This activity represents a critical perinatal window (during the first or second postnatal week in rodent pyramidal hippocampal neurons; Banke and McBain, 2006; Ben-Ari et al., 1989; Khazipov et al., 2004), setting the stage for lifelong excitatory/inhibitory balance and local circuit homeostasis (Amin et al., 2017; Ben-Ari, 2002; Cellot and Cherubini, 2014; Ganguly et al., 2001). Given that AIS damage due to disease or injury leads to nervous system dysfunction (Buffington and Rasband, 2011; Schafer et al., 2009), AIS-associated functions and the GABA polarity switch may functionally interact.

To understand physiological and functional interactions between proteasome complexes and the AIS at early stages of neuronal maturation, we investigated mechanisms regulating proteasome distribution and function relevant to the timing of AIS formation and the GABA polarity switch. To do so, we monitored Ecm29-associated proteasome transport behavior in growing axons, with or without an intact AIS. We observed that Ecm29 associates with the AIS anchoring protein AnkG and is required for proteasome retention in the AIS region. Maturing mouse hippocampal or cortical neurons lacking Ecm29 exhibited aberrant accumulation of the Na-K-Cl cotransporter (NKCC1) in the somatodendritic compartment and at the AIS, leading to prolonged GABAergic excitation and a precocious shift in AIS position. In contrast, blocking NKCC1 activity by treating young neurons with bumetanide (BUM) rescued hyperactivity seen in Ecm29 knockout (KO) neurons. Phenotypically, mice lacking Ecm29 exhibited increased susceptibility to chemically induced seizures. We demonstrate that proper maturation and excitability in developing neurons require AIS- and Ecm29-controlled proteasome distribution and function.

Results

The AIS controls polarized distribution of Ecm29 and proteasomes in maturing hippocampal and cortical neurons

Newborn hippocampal and cortical neurons develop an intracellular proteasome gradient at a nascent axon via a microtubule-based transport mechanism. However, it remains unclear whether maturing neurons later rely on the AIS to maintain asymmetric proteasome distribution throughout a neuron's lifetime. To determine this, we assessed distribution of proteasome complexes in 5-DIV rat neuronal cultures, a time point after establishment of AIS structure, from both the cerebral cortex and hippocampus using fluorescent staining with antibodies against the proteasome regulatory particle base subunit Rpt5 and the AIS marker AnkG. As shown in Fig. 1 A, levels of proteasome subunits in axonal compartments of 5-DIV neurons were significantly lower than in dendritic-somatic compartments, with signal intensity declining steeply at or beyond the AIS region. We then asked whether asymmetric proteasome distribution requires an intact AIS. To do so, we used siRNA knockdown of the AIS scaffold protein AnkG or establishment of ischemia-like conditions in 5 DIV cultured neurons to partially disrupt the AIS (Fig. 1, A and B). Both approaches led to significantly lower levels (10–30% relative to wild-type) of AnkG signals along the proximal axon (Fig. 1, A, B, and E). Moreover, relative to wild-type control axons, AnkG-knockdown axons exhibited more evenly distributed Ecm29/proteasome staining, without accumulation of Ecm29/proteasomes in the proximal axon (Fig. 1, A and B). We observed similar alterations in Ecm29/proteasome distribution in 5-DIV cultures after 30 min of oxygen glucose deprivation (OGD), a modified ischemia-like protocol that causes partial disassembly of the AIS structure but does not promote cell death in this context (Fig. 1, A and B; and Fig. S1). These findings support the idea that localization of both Ecm29 and proteasome is governed by AIS formation.

We next monitored transport of proteasome complexes using the selective proteasome-labeling agent MV151 in 5-DIV cultured neurons to evaluate local proteasome dynamics in the AIS. To do so, we stained living ∼5–7-DIV neurons with antibodies to the extracellular domain of the axonal cell adhesion molecule neurofascin-186 (NF-186) to locate AIS position (Fig. 1, C and D). Analysis of MV151-labeled proteasomes in control hippocampal or cortical neurons revealed that ∼20% of mobile proteasomes anterogradely traversed the AIS region, while ∼15% reversed their movement at or in front of the AIS, and most (∼65%) proteasomes within the AIS region were stationary (Fig. 1, C and D). Note that proteasome transport is dependent on the adaptor Ecm29, as most, if not all, MV151-labeled proteasomes along axons of Ecm29 KO ($Ecm29^{-/-}$) neurons were stationary (Fig. 1, C and D; and Video 1). On the other hand, treatment of control neurons with AnkG-siRNA significantly increased the proportion of proteasomes undergoing anterograde movement through the proximal axon region (to up to 40%), while the proportion of stationary proteasomes decreased (Fig. 1 D). In contrast, disrupting actin filaments by treating 5-DIV cultures with 1 µM latrunculin A for 6 h had no significant effect on Ecm29/proteasome retention at the AIS, nor did it decrease AnkG staining in the proximal axon region (Fig. 1, C–E). Together, these findings suggest that Ecm29/proteasome complexes are tethered to the AIS via unknown mechanisms, not actin filaments.

AnkG interacts with Ecm29 to tether proteasomes to the AIS

The proteasome adaptor Ecm29 may enable tethering of mobile proteasomes to the AIS by interacting with the AIS scaffold protein AnkG. To assess this possibility, we first investigated interactions between Ecm29-containing complexes and AnkG using in vitro GST pulldown assays (Fig. S2). Full-length Ecm29 associated with AnkG, the proteasome subunit Rpt1, and the motor-related proteins Arp1 and KIF5B. Moreover, in vitro domain mapping revealed that the Ecm29 N-terminal region

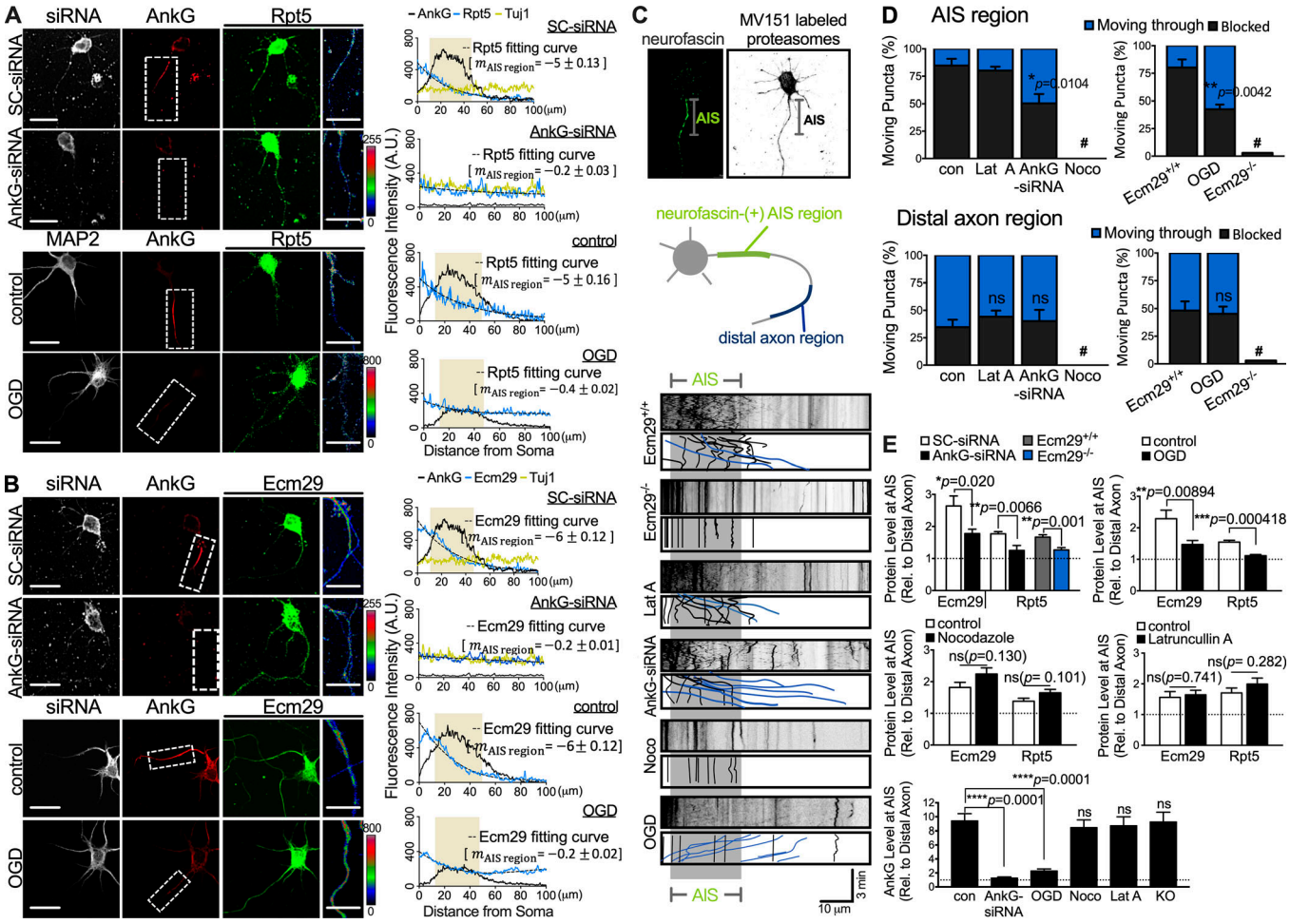

Figure 1. **Asymmetric proteasome distribution requires AIS integrity. (A and B)** Either AnkG knockdown or induction of ischemia-like conditions (OGD) impairs AIS structure and proteasome distribution in cultures of mouse neurons on 5 DIV. Images of hippocampal neurons transfected with scrambled control (SC-siRNA) or AnkG-siRNA 30 min after plating, followed by immunostaining for the AIS marker AnkG (red), proteasome subunit Rpt5 (green, A), or the proteasome adaptor Ecm29 (green, B) at 5 DIV. Rightmost panels show regions of interest (dashed boxes) of the AIS represented at higher magnification, with Rpt5 (A) or Ecm29 (B) staining intensity indicated by a linear pseudocolor scale. Plots at right reveal a more uniform distribution (reflected by flatter slopes) of Rpt5 (blue trace, A) and Ecm29 (blue trace, B) across the AIS region and distal axon following AnkG knockdown or after 30 min of OGD conditions. Scale bar, 20 µm. Traces of neuron-specific class III β-tubulin (Tuj1) show that the microtubule bundle was not altered following AnkG knockdown. Traces represent averages of >50 cells per group from three independent experiments. *m*, slope of the intensity profile of Rpt5 or Ecm29 across the AIS. **(C and D)** MV151-labeled proteasomes are retained in the AIS region. **(C)** Top: Representative image showing a 5-DIV cortical neuron stained with neurofascin antibody and MV151 to visualize AIS position and proteasome movement, respectively, during live-cell imaging. Middle: Schematic showing position of the AIS (neurofascin-positive segment) and distal axon regions, defined as the axonal segment 60–80 µm from cell body. Bottom: Representative kymographs (2 s/frame; 180 s) of MV151-labeled proteasomes in axons of 5-DIV neurons following treatments indicated at left. Corresponding color-coded trajectories plotted for a subset of MV151-labeled proteasomes (blue lines, particles moving through AIS region; black lines, particles blocked or static in the proximal axon). Static particles outside the AIS are not marked. **(D)** Summary histograms showing that either AnkG knockdown by siRNA-AnkG or ischemia-like conditions (OGD for 30 min) significantly increase the percentage of MV151-labeled proteasomes across the AIS (denoted as "moving through") in 5- or 6-DIV neurons. Note that treatment with the actin filament–depolymerizing agent latrunculin A (Lat A; 1 µM for 6 h) had no effect on proteasome transport, whereas the microtubule-disrupting agent nocodazole (Noco; 1 µM for 3 h) or Ecm29 KO ($Ecm29^{-/-}$) abolished all transport. con, Control $Ecm29^{+/+}$ group; #, no transport. Mean ± SEM, *n* = 20 cells per group from three independent experiments, 10–15 puncta each cell; *, P < 0.05; **, P < 0.01; ns, not significant compared with control group by unpaired *t* test. Scale bar, 20 µm. **(E)** Quantification of proteins at the AIS relative to those in the distal axon region in experiments conducted as described in C and D, except that 5-DIV cortical neurons were immunostained for Ecm29, Rpt5, and AnkG. Summary histograms show an even distribution of Ecm29 and Rpt5 over the AIS and distal axonal region in AnkG knockdown (AnkG-siRNA) neurons or OGD conditions, as indicated. Data represent mean ± SEM; *n* > 4 independent experiments, >50 cells per group; *, P < 0.05; **, P < 0.01; ****, P < 0.0001; ns, not significant compared with control group by unpaired *t* test (Ecm29 and Rpt5 panels), or by one-way ANOVA with Dunnett's multiple comparison test (AnkG panel).

(Ecm29ΔC) is essential for maximal association with these factors (Fig. S2 A). On the other hand, the AnkG C-terminal death domain and C-terminal tail were required for Ecm29 association, and the AnkG N-terminal membrane binding domain and spectrin binding domain (SBD) were necessary for association with proteasomes or motor proteins in brain tissue lysate and/or Neuro-2a cell lysate (Fig. S2, B and C; Barry et al., 2014).

Consistent with our observations in vitro (Fig. S2, A and B), we found that immunoprecipitated (IP) Flag-Ecm29 associated with 190AnkG-GFP in vivo when both were expressed

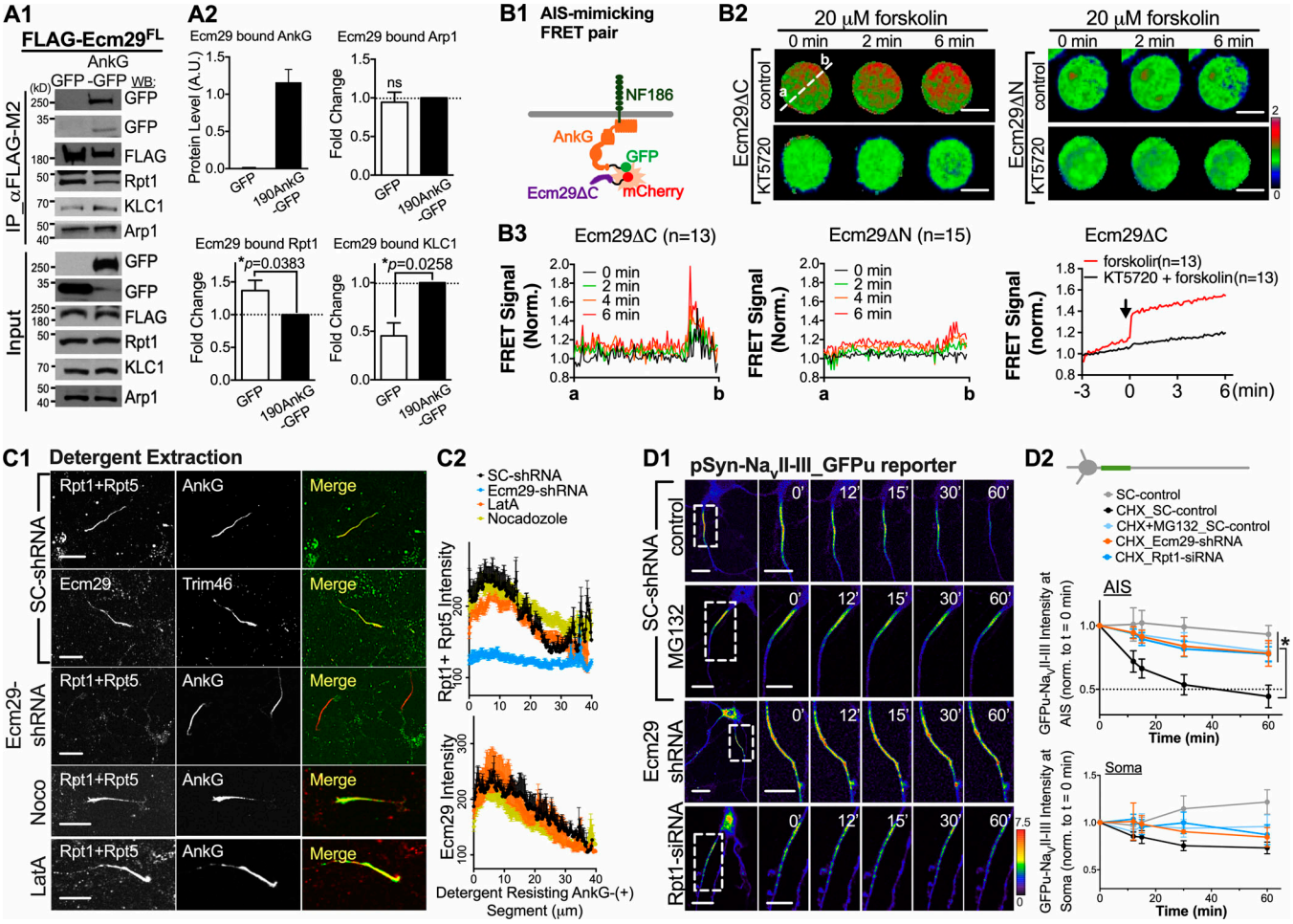

Figure 2. **Proteasome retention and local protein degradation in the AIS require Ecm29 interaction with AnkG. (A)** In vivo protein binding assays in HEK293T cells transfected with a plasmid encoding FLAG-tagged Ecm29$_{1–1,840}$ (FLAG-Ecm29^{FL}) and plasmids encoding 190AnkG-GFP (AnkG-GFP) or control GFP vectors, as indicated. Cell lysates were IP by FLAG M2 antibodies and blotted with indicated antibodies. Histograms at right show relative protein levels based on immunoblotting of GFP, Arp1, Rpt1, and KLC1 coIP by FLAG antibodies (±SEM; n = 4 independent experiments; *, P < 0.05; ns, not significant, by t test). **(B)** cAMP increases facilitate Ecm29–AnkG interaction. **(B1)** Schematic showing design of AIS-mimicking ratiometric FRET sensors. AIS molecular dock: NF-186. Donor molecule: 190AnkG-GFP. Acceptor molecule: Ecm29ΔC-mCherry or Ecm29ΔN-mCherry. **(B2)** Time-lapse FRET images of HEK293T cells co-transfected with plasmids encoding 190AnkG-GFP, NF-186-HA, and N- or C-terminal Ecm29-mCherry (Ecm29ΔC-mCherry or Ecm29ΔN-mCherry) in the presence of 20 μM forskolin, with or without 30 min of pretreatment with the PKA inhibitor KT5720, as indicated. White dashed line passes through the center of the cell, with points a and b as intersection points. Scale bar, 10 μm. **(B3)** Quantitative measurement of FRET signals (±SEM, n ≥ 13 cells for each group) at different times before and after addition of forskolin (20 μM) in experiments as described in B. Arrow in right panel denotes forskolin addition. Norm., normalized. **(C)** Ecm29 expression is required for proteasome association with the detergent-resistant AIS structure. **(C1)** Representative images of 7-DIV hippocampal neurons transfected with SC-shRNA or AnkG-targeting siRNA (AnkG-siRNA) at 3 DIV, with or without nocodazole (Noco; 1 μM for 3 h) or latrunculin A (Lat A; 1 μM for 6 h), followed by detergent extraction with 0.1% Triton X-100 at 37°C for 2 min before immunostaining for the AIS marker AnkG/Trim46 (red, merge panels), proteasome subunit Rpt1/Rpt5 (green, merge panels), and the proteasome adaptor Ecm29 (green, merge panels). **(C2)** Quantitative measurement of immunostaining intensities (±SEM, n = 15–35 cells) along AIS segments. **(D)** Local protein turnover at the AIS requires Ecm29 expression and proteasome activity. **(D1)** Images of 7-DIV hippocampal neurons expressing an AIS-located protein degradation reporter, Na$_V$II-III–tagged GFPu, showing more durable GFPu accumulation after MG132 pretreatment (2.5 μM, 30 min) or shRNA-mediated knockdown of Rpt-1 or Ecm29 expression, as indicated. Scale bar, 15 μm. **(D2)** Quantitative measurement of fluorescence intensities in the AIS (top panel) and soma (bottom panel) at different time points based on all experiments performed as described in D1 (±SEM, n > 6 cells for each group, one-way ANOVA followed by Dunnett's multiple comparison test. *, P < 0.05; ns, not significant).

ectopically in HEK293 cells (Fig. 2 A). To assess Ecm29–AIS interaction in a subcellular context that recapitulates AIS localization, we cotransfected HEK293T cells with plasmids encoding NF-186 together with a Förster resonance energy transfer (FRET) pair (190AnkG-GFP and Ecm29ΔC-mCherry). When the transmembrane protein NF-186 and AnkG protein are simultaneously ectopically expressed in HEK293T cells, NF-186 recruits AnkG protein to the plasma membrane and forms an AIS-like membrane domain (Hedstrom et al., 2007; Sherman et al., 2005). As shown in Fig. 2, B2 and B3, quantitation of FRET intensity along symmetrical cell axes confirmed AnkG protein association with the Ecm29 N-terminal, with FRET signals accumulating around the cell periphery, indicative of an AnkG/Ecm29 association beneath the plasma membrane (Fig. 2 B2).

That association in vitro and in vivo was potentiated by treatment with forskolin, a cAMP-elevating factor known to induce neuronal maturation (Fig. 2, B2 and B3; and Fig. S2 C; Fujioka et al., 2004). In contrast, when we cotransfected HEK293T cells with the Ecm29 C-terminal (see Ecm29ΔN in Fig. 2, B2 and B3), which does not interact with the AIS (Fig. S2 A), we did not observe elevated FRET signals around the cell periphery with or without forskolin treatment. These findings support the idea that AnkG can tether Ecm29 complexes to an AIS-like membrane domain.

To verify that endogenous Ecm29 associates with AIS proteins in maturing neurons, we used structured illumination microscopy (SIM; Fig. S2, D–F) and antibodies specifically targeting the AnkG C-terminal domain (AnkG antibody H215). We observed that Ecm29 colocalizes with AnkG at the AIS of 7-DIV neurons (Pearson's correlation coefficient ≥0.67; Fig. S2, D and E). Based on AnkG domain mapping studies (Fig. S2 B), we also compared staining patterns of Ecm29 and proteasomes along axons with that of AnkG using a different antibody (AnkG antibody clone 463) that targets the proteasome-interacting AnkG N-terminal SBD domain. Spatially, when expressed in hippocampal neurons, the AnkG N-terminal SBD reportedly exhibits a periodic staining pattern due to direct association with the evenly spaced submembrane βIV-spectrin lattice and the spectrin lattice is spatially constrained by periodic actin bands beneath the AIS membrane (Leterrier et al., 2015). In comparison, staining patterns of the AnkG C-terminal domain, which extends into the cytosol, are disordered along neuronal processes (Leterrier et al., 2015; Xu et al., 2013; Zhong et al., 2014). Indeed, SIM images revealed a similar spatial organization with a periodicity of ∼190 nm for proteasome subunits (such as Rpt1, Rpt5, and 20S core particles [20S CP]) as well as the AnkG N-terminal domain, but not for the AnkG C-terminal domain, Ecm29, or signals outside the AIS region (Fig. S2 F). These findings further support the idea that in neurons, proteasomes are tethered to the AIS.

The AIS structure and associated proteins are stable and resistant to membrane and cytoskeletal perturbations; moreover, AIS-restricted and AnkG-interacting proteins are retained at the AIS after detergent extraction (Garrido et al., 2003; Huang et al., 2017). Thus, we used detergent extraction of cells in hippocampal culture at 7 DIV to confirm association of the AIS protein AnkG/Trim46 with Ecm29 or proteasome subunits (Fig. 2 C). For this analysis, we performed extraction with 0.1% Triton X-100 at 37°C for 2 min to ensure that factors firmly, but not weakly, interacting with the AIS remained intact. Immunofluorescence (IF) staining of the cultured cells after extraction revealed that Ecm29 and proteasome proteins such as Rpt1 and Rpt5 were retained with AIS structure proteins in control neurons (Fig. 2 C). To assess whether proteasome tethering to the AIS was perturbed by Ecm29 loss, we knocked down Ecm29 using shRNA at 3 DIV and analyzed staining intensity of proteasome subunits retained in the AIS region after extraction at 7 DIV. Ecm29 knockdown in hippocampal cultures significantly decreased the level of proteasome subunits retained at the AIS (Fig. 2 C), suggesting that Ecm29 not only mediates proteasome transport along microtubules but participates in proteasome tethering to the AIS. Moreover, neither the microtubule-disrupting agent nocodazole nor the actin filament-depolymerizing agent latrunculin A was sufficient to reduce levels of Ecm29 and proteasomes tethered to AnkG (Fig. 2 C), consistent with our observation in the proteasome transport experiment (Fig. 1, C–E). Overall, these findings support the idea that Ecm29 and proteasomes physically associate with AIS structural proteins in neurons.

Proper protein turnover at the AIS requires Ecm29 expression

Our work suggests that Ecm29-associated proteasome localization at the AIS may function to control local protein turnover. To examine the possibility, we investigated protein degradation activity in the AIS region by tagging the AnkG binding loop (Na_VII-III; Dumitrescu et al., 2016; Grubb and Burrone, 2010) with a short-lived form of GFP (GFPu; Bence et al., 2005) to establish a reporter of AIS-targeted protein degradation. Hippocampal neurons at 7 DIV were transfected with the Na_VII-III–tagged GFPu construct and, at 10 DIV, subjected to live-cell fluorescence microscopy imaging in the presence of the protein synthesis inhibitor cycloheximide (10 µM). As shown in Fig. 2 D, the average half-life of the AIS-localized, Na_vII-III–tagged GFPu in 10-DIV wild-type neurons was ∼35 min or >2 h in the absence or presence of the protein degradation inhibitor MG132 (2.5 µM, 30-min pretreatment), respectively. However, in 10-DIV Ecm29 KO neurons, we observed a significantly longer Na_vII-III–tagged GFPu half-life of >2 h in the AIS region in the absence of MG132 (Fig. 2 D2). Similarly, neurons with suppressed proteasomal activity due to either siRNA-mediated knockdown of the proteasome subunit Rpt-1 or MG132 (2.5 µM, 30 min) pretreatment showed a >2 h Na_VII-III–tagged GFPu half-life at 10 DIV (Fig. 2 D), supporting the idea that local protein turnover at the AIS is regulated by Ecm29 association with the proteasome.

NKCC1 accumulates in the AIS of Ecm29 KO neurons

It is generally accepted that early in development, GABAergic transmission is excitatory due to a high ratio of cation-chloride cotransporters (NKCC1:KCC2), which govern intracellular chloride concentrations, $[Cl^-]_i$, in immature neurons (Alvarez-Leefmans et al., 1988; Payne et al., 1996; Rivera et al., 1999; Rohrbough and Spitzer, 1996; Russell, 2000). The reversal dominance from NKCC1 to KCC2 expression in rodent cortex occurs in the first postnatal week (Yamada et al., 2004), and the depolarizing to hyperpolarizing GABAergic switch occurs in hippocampus and cortex at around P5 (Ben-Ari et al., 1989; Swann et al., 1989; Watanabe and Fukuda, 2015). However, how NKCC1 levels are down-regulated either globally or locally during the excitatory-to-inhibitory GABA transition remains unclear. To ascertain whether Ecm29-associated protein turnover contributes to the balance of global and local channels required for the GABA switch, we first analyzed expression patterns of specific membrane receptors/channels associated with GABAergic neurotransmission in lysates of mouse embryonic day 16 (E16) to P19 cerebral cortex, as well as in 7-DIV hippocampal/cortical cultures (Figs. 3, S3 A, and S4). Of 18 proteins assessed, one channel receptor, NKCC1, exhibited altered expression in lysates made from early postnatal Ecm29 KO

(Ecm29$^{-/-}$) cerebral cortex relative to wild-type (Ecm29$^{+/+}$; Fig. 3 B). Based on analysis of wild-type mouse brain lysates, cortical NKCC1 protein levels were higher at embryonic and postnatal days before P4 and then gradually decreased thereafter (Fig. 3 A). In contrast, Ecm29$^{-/-}$ neurons expressed significantly higher overall amounts of NKCC1 protein compared with wild-type neurons and exhibited a slower rate of decline in NKCC1 protein levels across experimental time points from P1 to P16 (Fig. 3 A). We also examined the fraction of proteins localized to the cell membrane by biotinylation of acute brain slices at P0 and P14 followed by streptavidin pull-down of surface-bound NKCC1. As shown in Fig. 3 B, Ecm29$^{-/-}$ brains exhibited significantly higher levels of NKCC1 protein on the plasma membrane relative to control wild-type brains, supporting the idea that NKCC1 accumulates in Ecm29$^{-/-}$ perinatal brains.

We then asked if Ecm29 loss altered local NKCC1 abundance using IF staining (Figs. 3 C and S4). Indeed, we observed that intensity and density of NKCC1 clusters significantly increased (~1.45× higher) in the AIS region of 7-DIV Ecm29$^{-/-}$ compared with wild-type neurons (Fig. 4, C1 and C3; and Fig. S4 A). This finding is in agreement with the reduced protein turnover rate observed in the AIS region of Ecm29$^{-/-}$ neurons (Fig. 2 D), indicating that Ecm29/proteasome-mediated protein degradation contributes, at least in part, to maintaining the proper NKCC1 content in the AIS. To confirm these findings, we used pulse-chase analysis of NKCC1 stability in wild-type and Ecm29 KO neurons (Fig. 3 D). To do so, cells were pulse-labeled for 24 h with the noncanonical methionine analogue L-azidohomoalanine (AHA) in methionine-free medium and chased specifically for NKCC1 protein by immunoprecipitation with NKCC1 antibodies. As shown in Fig. 3 D, Ecm29 loss increased NKCC1 stability, increasing its half-life in Ecm29 KO hippocampal neurons to >9 h, significantly longer than the ~6 h seen in wild-type neurons. This enhanced stability was rescued by ectopic expression of proteasome/AnkG binding Ecm29 (Ecm29ΔC; Fig. 3, D2 and D3). Potential effects on total protein synthesis were excluded, as amounts and rates of synthesis of AHA-labeled proteins were comparable in wild-type and Ecm29 KO neurons (Fig. S3, B and C). Overall, these findings support the idea that Ecm29 modulates the rate of NKCC1 turnover in immature hippocampal neurons.

We also used real-time RT-PCR to exclude the possibility that NKCC1 accumulation was due to changes in transcription. Analysis showed comparable abundance and the same pattern of modest, gradual decline for NKCC1 mRNA in lysates from wild-type and Ecm29$^{-/-}$ cerebral cortex from P1 to P14 (Fig. S3 C). Moreover, developmental up-regulation of KCC2 mRNA and protein levels in brain lysates was also comparable between genotypes, despite the observation that dendritic staining of KCC2 protein was slightly higher (~1.14×, did not reach statistical significance) in 7-DIV Ecm29$^{-/-}$ compared with wild-type neurons (Fig. 3, C2 and C3; and Fig. S4 B). Specific NKCC1 protein accumulation may be a consequence of different spatiotemporal expression and/or subcellular patterns of NKCC1 and KCC2 proteins (Côme et al., 2019; Watanabe and Fukuda, 2015), as KCC2 protein levels on the plasma membrane were low in immature hippocampal neurons, and KCC2 protein was distributed exclusively in the axon compartment in both control and Ecm29$^{-/-}$ neurons at 7 DIV (Fig. 3, A and B; and Fig. S4 B; Báldi et al., 2010; Chamma et al., 2013; Gulyás et al., 2001; Szabadics et al., 2006). Overall, our findings suggest that NKCC1 protein levels in maturing neurons are governed by changes in stability due to association with Ecm29, rather than rate of synthesis.

GABAergic excitation is prolonged in immature Ecm29 KO neurons

To address how protein turnover governs AIS activities, we focused on the excitatory-to-inhibitory switch of neuronal GABA responsiveness in maturating cultured hippocampal neurons. Notably, that switch occurs concomitant with AIS formation at the proximal axon, and both events occur between 5 and 14 DIV in hippocampal/cortical cultures. Within this time window, we asked whether Ecm29 expression was required for the GABA polarity switch and AIS formation to occur in a timely manner. To do so, we used cells harboring a genetically encoded ratiometric Cl^- sensor (PalmPalm-ClopHensor; Arosio et al., 2007, 2010) to assess near-membrane chloride dynamics in response to GABA transmission in wild-type and Ecm29 KO hippocampal/cortical neurons at different time points (Fig. 4). The intensity ratio (denoted in the cyan-to-red ratio [R_{Cl-}] index) is calculated as chloride-suppressing cyan fluorescence divided by control DsRed fluorescence of the PalmPalm-ClopHensor, and its value is inversely correlated with $[Cl^-]_i$ under physiological (~7.4) pH. Specifically, R_{Cl-} increases or decreases indicate chloride efflux or influx, respectively, upon $GABA_A$ receptor activation. For wild-type cortical neurons at 5 DIV, we observed detectable chloride efflux upon focal GABA application to dendritic processes and to proximal (the AIS region) and distal axons (Fig. 4, A1 and A2). Efflux activity switched to influx after 7 DIV (Fig. 4 A2). However, the timing of this switch was delayed to ~9 DIV in Ecm29 KO neurons (Fig. 4 A2), and the percentage of Ecm29 KO cells exhibiting excitatory GABA transmission was significantly higher than that observed in wild-type neurons (Fig. 4, B and C). The pH index, calculated as the ratio of GFP to cyan, also changed following the same pattern (data not shown). The GABA polarity switch from excitation to inhibition was controlled by levels of NKCC1, as pretreating 5-DIV neurons with the NKCC1 inhibitor BUM (10 µM) for 16 h resulted in an early chloride-dependent switch in both wild-type and Ecm29 KO neurons (Fig. 4, B–D). Moreover, prolonged excitatory GABA responses seen in Ecm29 KO neurons were ameliorated by ectopic Ecm29 expression (Fig. 4, A and D), supporting the idea that Ecm29 expression and NKCC1 activity are required for proper GABAergic neurotransmission in young neurons. We also observed that a majority (>95%) of both control and Ecm29 KO neurons had an AnkG/Trim46-positive segment developed at proximal axons in 5-d cultures (Fig. S4, F and G), suggesting that the AIS may be structurally intact but functionally aberrant after Ecm29 loss.

We next asked whether Ecm29 loss promotes hyperresponsiveness to excitatory GABAergic transmission. To do so, we compared GABA-induced calcium transients between wild-type and Ecm29 KO cortical neurons during and after the excitatory-to-inhibitory GABA switch (5–14 DIV; Fig. 4 E).

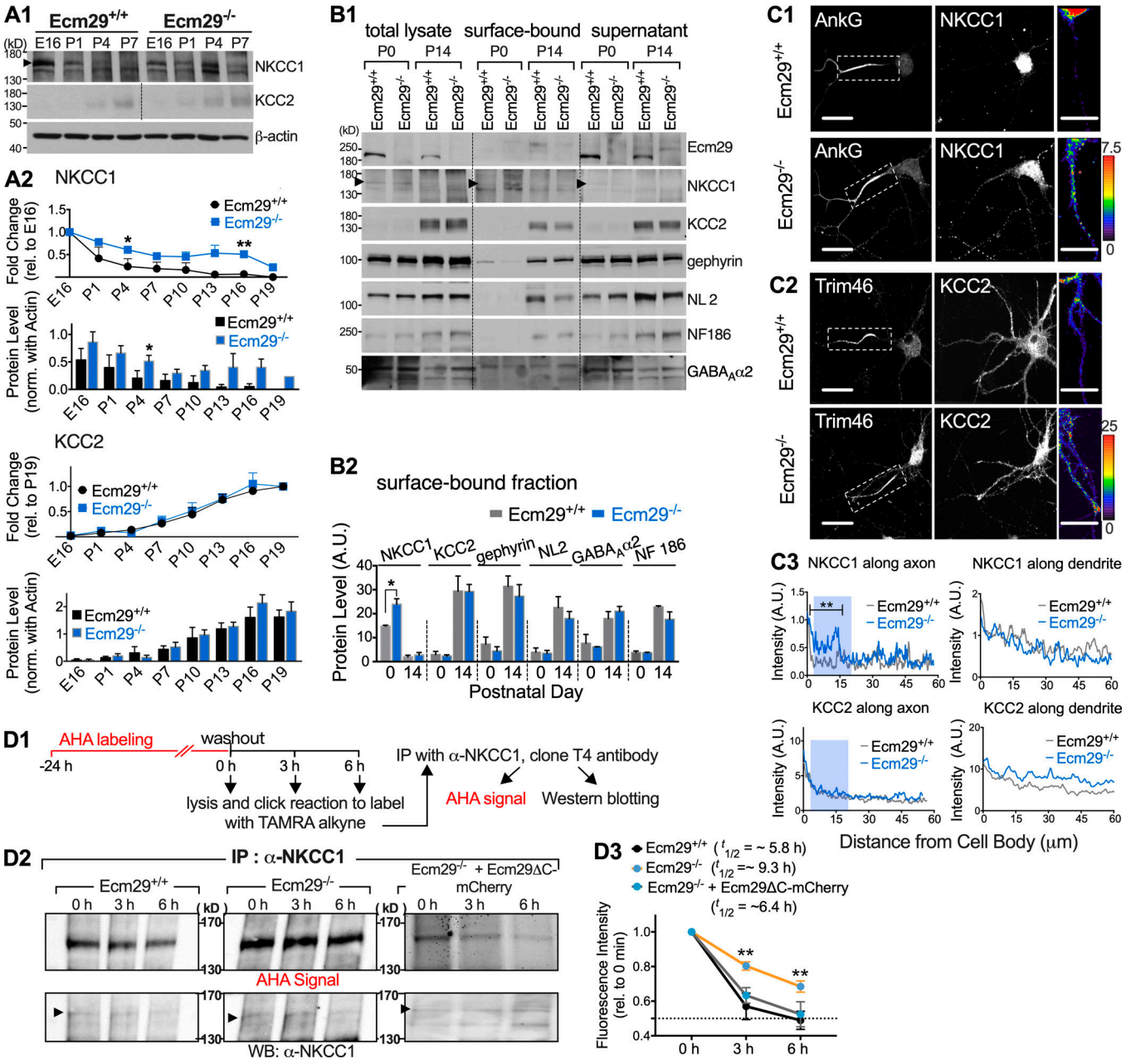

Figure 3. **Ecm29 KO neurons exhibit aberrant NKCC1 accumulation. (A)** Total NKCC1 levels increase in Ecm29$^{-/-}$ KO brain cortical lysates. **(A1)** Western blots of lysates showing NKCC1 and KCC2 protein expression at indicated developmental stages. Arrowhead denotes immunoreactive bands corresponding to NKCC1. **(A2)** Quantification of protein levels from all experiments performed as described in A1 at different time points and compared with corresponding levels at both E16 and P19 (top panel) or normalized to actin as an internal control (bottom panel). Data represent mean ± SEM from more than three independent experiments; *, P < 0.05, multiple *t* tests. rel., relative. **(B1)** Cell surface biotinylation assay of brain tissue lysates at indicated developmental stages. Representative Western blot of total lysate, streptavidin pull-down (surface-bound), and supernatant fractions probed with antibodies to Ecm29, NKCC1, KCC2, the inhibitory synapse markers gephyrin and Neuroligin-2 (NL2), and the AIS-associated factors NF-186 and GABAa α2 receptors, as indicated. Arrowhead denotes immunoreactive bands corresponding to NKCC1. **(B2)** Histogram showing quantitation of proteins (±SEM; *n* > 3 independent experiments; *, P < 0.05, multiple *t* tests for each factor) in the surface-bound fraction. **(C)** Ecm29$^{-/-}$ KO neurons exhibit altered NKCC1 accumulation at the AIS. **(C1 and C2)** Representative confocal images of 7-DIV neurons coimmunostained with AnkG and NKCC1 (C1) or Trim46 and KCC2 (C2) antibodies, as indicated. Rightmost panels show regions of interest (dashed boxes) of the AIS represented at higher magnification, with NKCC1 (C1) or KCC2 (C2) staining intensity indicated by a linear pseudocolor scale. Bar: 20 µm. **(C3)** Traces from experiments performed as described in (C1) and (C2), showing NKCC1 and KCC2 staining along the first 60-µm region of axonal (right panels) and dendritic (left panels) processes. Light blue rectangles mark AnkG/Trim46-(+) AIS regions. Data points represent signal intensities (±SEM, *n* = 75–92 neurons for each set of experiments; **, P < 0.01, *t* test). **(D)** NKCC1 half-life increases in Ecm29$^{-/-}$ KO cortical cultures. **(D1 and D2)** Paradigm and representative blots for pulse-chase experiments on AHA-labeled, newly synthesized proteins in 5-DIV cortical cultures of wild-type, Ecm29 KO, or Ecm29 KO transfected with plasmid encoding Ecm29ΔC-mCherry, followed by AHA signal detection (top panel, D2) and Western blotting (bottom panel, D2) of the IP sample with an NKCC1 antibody. Arrowhead denotes immunoreactive bands corresponding to NKCC1. **(D3)** Summary of AHA signal intensity normalized to that of the corresponding Western blot bands (±SEM, *n* = 3 independent experiments; **, P < 0.01, *t* test) at different time points as indicated. NKCC1 protein $t_{1/2}$ was calculated by exponential decay.

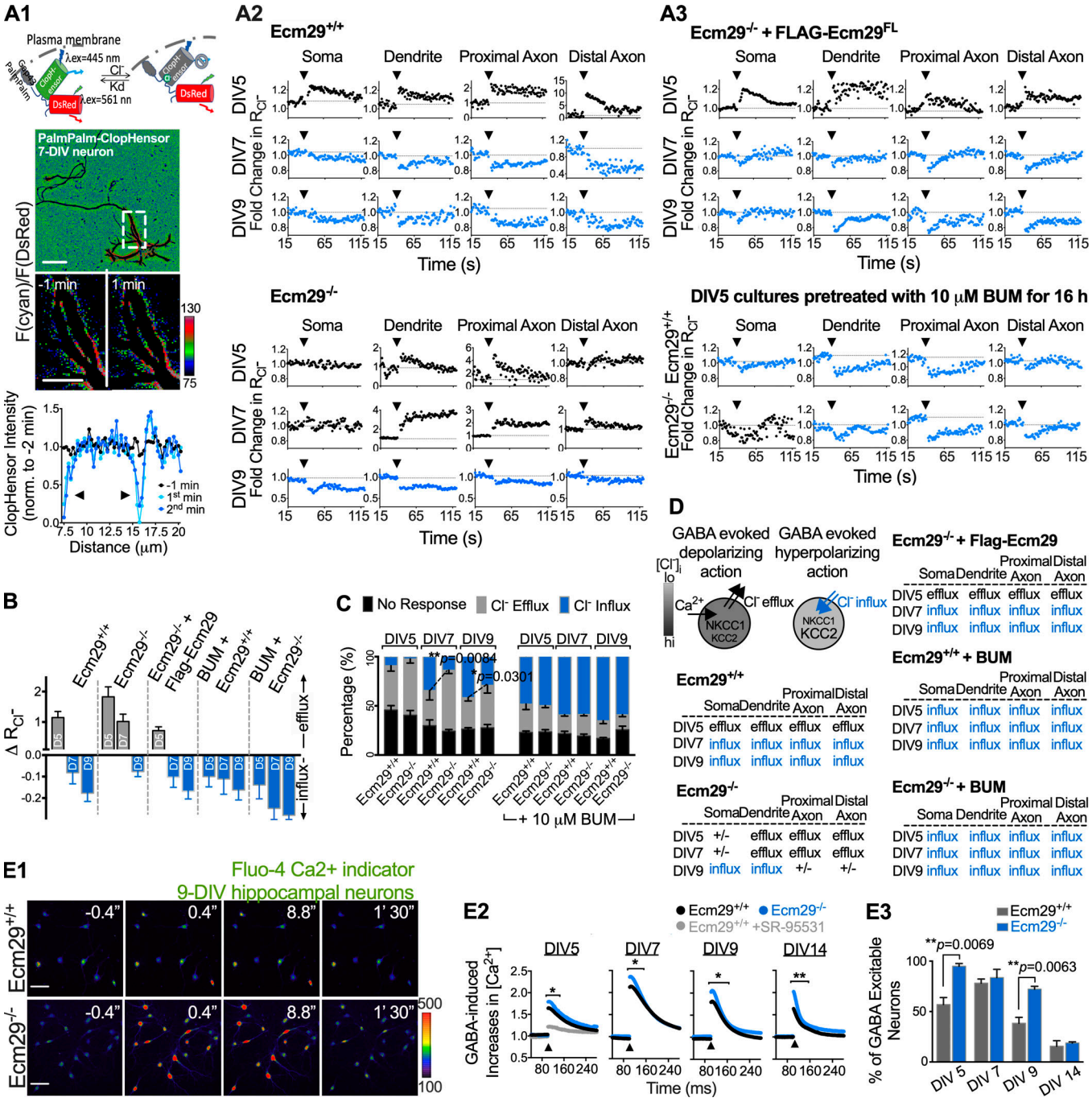

Figure 4. **Neurons lacking Ecm29 exhibit a delayed GABAergic excitation-to-inhibition switch and an altered GABA-induced calcium response.** **(A)** Ratiometric fluorescent imaging of hippocampal or cortical neurons transfected with the genetically encoded, membrane-bound chloride indicator PalmPalm-ClopHensor to assess chloride fluxes. **(A1)** Top: Schematic illustrating Cl^--dependent static quenching of ClopHensor fluorescence upon excitation with blue laser (λex = 445 nm). Kd, dissociation constant. Middle: Representative images depicting chloride levels, as indicated by the PalmPalm-ClopHensor signal calculated as the ratio of cyan to DsRed fluorescence (F(cyan)/F(DsRed)) acquired from a 7-DIV neuron. Bottom: Background substrate images and traces corresponding to the outlined region in the middle panel, indicating inward chloride transitions (arrows) after 20 μM focal GABA application. Scale bar, 20 μm. **(A2)** Representative traces depicting GABA-induced fluxes in wild-type ($Ecm29^{+/+}$) and Ecm29 KO ($Ecm29^{-/-}$) neurons at 5–9 DIV, before and after 20 μM focal GABA application. Blue traces denote chloride influxes; black traces denote chloride effluxes or no response. Arrows indicate time points of focal GABA addition. **(A3)** Experiments similar to A2, except cells were transfected with plasmid encoding FLAG-tagged $Ecm29_{1–1,840}$ ($Ecm29^{FL}$) or pretreated with the NKCC1 inhibitor BUM (10 μM; for 16 h before experiments) as indicated. **(B)** Averaged GABA-induced changes in the cyan-to-DsRed ratio (denoted ΔR_{Cl-}) at the proximal axon region reveals a prolonged excitatory period in Ecm29 KO ($Ecm29^{-/-}$) neurons in all experiments performed as described in A. Data represent mean ± SEM ($n \geq 25$ cells for each group from at least three independent experiments). **(C)** Summary of percentages of neurons exhibiting different GABA-induced fluxes in the proximal axon region in cultures described in A. Data points connected by dashed lines differ significantly (mean ± SEM, $n = 90$ cells; *, $P < 0.05$; **, $P < 0.001$, compared with corresponding sets in control wild-type ($Ecm29^{+/+}$) neurons, based on multiple t tests). **(D)** Schematic showing GABA-induced chloride fluxes for different cell regions, and table summarizing timing of the switch in GABA response from chloride efflux to influx for each indicated

group. **(E1 and E2)** Young Ecm29$^{-/-}$ hippocampal neurons (5–9 DIV) exhibit a higher Ca^{2+} influx than wild-type Ecm29$^{+/+}$ neurons in response to a GABA stimulus (20 µM) as indicated in representative images (E1, 9-DIV cultures) and traces (E2, 5–14-DIV cultures), based on analysis with the calcium-sensitive indicator Fluo-4. *n* = 25–175 cells; *, P < 0.05; **, P < 0.001, compared with the wild-type (Ecm29$^{+/+}$) group by multiple *t* tests. Scale bars, 50 µm. Arrow denotes addition of GABA. (**E3**) Histograms show average percentages of neurons exhibiting Ca^{2+} responses to focal GABA application. Data represent mean ± SEM, *n* = 25–175; **, P < 0.01, *t* test.

Amplitudes of calcium flux in ∼5–14-DIV neurons were assessed using the fluorescent Ca^{2+}-sensitive dye Fluo-4. GABA-induced calcium transients in 5-DIV neurons were primarily reflected by GABA-evoked current and activation of L-type calcium channels and the $GABA_A$ receptor, as treating cells with a competitive and selective $GABA_A$ receptor antagonist SR95331 or a L- and T-type calcium channel inhibitor mibefradil, but not T-type calcium channel blocker $NiCl_2$, eliminated those responses (Fig. S5). As shown in Fig. 4, E2 and E3, the GABA-induced Ca^{2+} response in wild-type neurons peaked at 7 DIV, declined gradually from 9 to 11 DIV, and then returned to basal levels before 14 DIV. This profile of Ca^{2+} entry triggered by GABA is highly consistent with the above-mentioned excitatory response to GABA seen in wild-type neurons. However, Ecm29 loss potentiated GABA-induced calcium activities, as we observed greater Ca^{2+} induction (1.2-fold increase) in Ecm29 KO neurons through the 5–14-DIV time period relative to activity seen in wild-type neurons (Fig. 4 E). Supporting our finding that Ecm29 KO neurons show a delay in hyperpolarizing chloride influx (Fig. 3), most (∼73%) Ecm29 KO neurons remained excitable by GABA at 9 DIV (Fig. 4 E3).

Ecm29 KO mice exhibit increased susceptibility to chemically induced seizures

Given that mice harboring mutations causing elevated NKCC1 expression or AIS dysfunction often develop seizure hypersusceptibility (Dzhala et al., 2010; Wang et al., 2017a; Wimmer et al., 2010a, 2010b), we asked whether Ecm29 expression can protect against seizure onset in young adult (∼3-mo-old) mice. We hypothesized that prolonged NKCC1 expression/excitatory GABA responsiveness in Ecm29-deficient immature neurons puts mice at higher risk of seizure (see Video 2 for an example of spontaneous onset of absence seizures/partial seizures observed in an Ecm29 KO mouse in a home-cage environment). To assess this possibility, we evaluated epileptogenesis by treating Ecm29 KO and wild-type mice with two different chemoconvulsants, flurothyl or pentylenetetrazole (PTZ). As shown in Fig. 5 A, the timing of the first myoclonic jerk and onset of a generalized seizure following 10% flurothyl exposure was significantly more rapid in Ecm29 KO relative to wild-type mice in all experimental trials (Fig. 5, A1 and A2). Ecm29 KO mice exhibited significantly higher levels of symptom severity and progression, as reflected by a much shorter onset latency of both myoclonic and generalized clonus (GC) in the subsequent trial, than that seen in wild-type mice (Fig. 5, A3 and A4). In addition, such increased susceptibility of Ecm29 KO mice was accompanied by an increased mortality rate after six exposure trials (Fig. 5 A5). Similar hypersusceptibility was observed in a PTZ-induced acute seizure model, in which we used a nonlethal dose (60 mg PTZ/kg; Fig. 5 B3) sufficient to provoke more frequent myoclonic seizures in Ecm29-deficient than in wild-type young adult mice (Fig. 5 B), supporting the idea that Ecm29 loss renders young adult mice hypersusceptible to seizure.

In parallel, we asked whether decreasing NKCC1 activity at particular perinatal time periods (such as P7, which coincides with the GABA switch) and late juvenile age (∼7 wk; P50) would protect mice from effects of Ecm29 loss. To do so, we administered the potent NKCC1 inhibitor BUM at an effective concentration (0.2 mg/kg body weight; once per day) i.p. for seven consecutive days. Control and BUM-treated mice were then exposed to flurothyl at a juvenile age (P35) or subjected to the PTZ kindling at P60 (both protocols reliably evoked seizures in wild-type mice, with a low [<20%] mortality rate; Fig. 5, A6 and C). We found that administering BUM to pups from P7 to P14 ameliorated effects of Ecm29 deficiency-dependent hypersusceptibility to both flurothyl-induced and PTZ-induced seizures in juvenile mice (Fig. 5, A6 and C1), while BUM administration at late juvenile (P50) was less effective compared with the treatment at perinatal age (Fig. 5 C2). Surprisingly, BUM administration to wild-type mice at perinatal (P7) or late juvenile (P50) ages was not protective, and instead animals exhibited a subtle increase in susceptibility to PTZ-induced seizures (Fig. 5 C), suggesting that proper neuronal responsiveness requires a fine balance in $[Cl^-]_i$ homeostasis at neonatal or early adult stages.

NKCC1 inhibition rescues aberrant neuronal excitability and AIS position phenotypes in developing Ecm29 KO neurons

NKCC1 accumulation (Fig. 3) and seizure hypersusceptibility (Fig. 5) due to Ecm29 loss prompted us to assess the relationship between neuronal excitability and Ecm29 expression. To do so, we first assessed innate basal electrical properties and behaviors of cell membranes, including resting membrane potential (RMP), membrane input resistance, membrane capacitance, and AP amplitude and current/voltage threshold of layer V pyramidal neurons of the medial prefrontal cortex (mPFC) in brain slices obtained from perinatal (P7–P9) mice (Fig. 6 A1). We found that overall membrane sodium channel homeostasis in Ecm29-deficient neurons was maintained at a constant level, equivalent to that seen in wild-type cells, based on comparable values seen for RMP and AP parameters in both genotypes (Fig. 6 A2). However, Ecm29 loss significantly increased spike number and frequency in mPFC layer V neurons in response to injection of depolarizing current (Fig. 6, B1 and B2), indicating hyperexcitability in Ecm29 KO neurons. Importantly, NKCC1 inhibition following bath-based BUM treatment (10 µM, 1 h) ameliorated aberrant excitability seen in Ecm29-deficient mPFC layer V neurons (Fig. 6, B1 and B2), supporting our hypothesis that altered NKCC1 accumulation in perinatal neurons underlies hyperexcitability of Ecm29-deficient neurons.

Finally, given AIS structural plasticity in response to early, chronic changes in neuronal excitation (Berger et al., 2018;

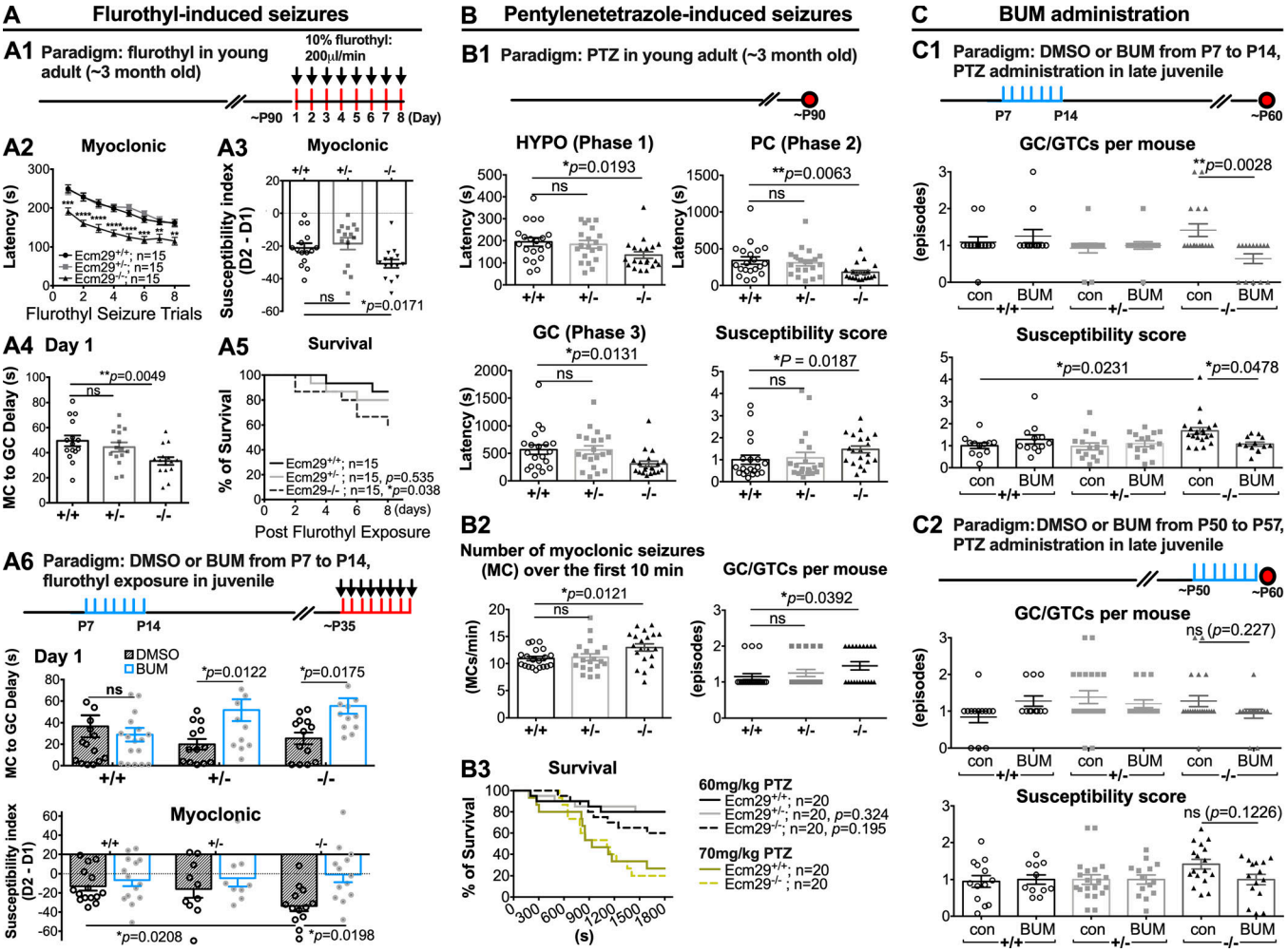

Figure 5. **Ecm29 KO mice exhibit increased seizure susceptibility. (A)** Ecm29 homozygous KO mice exhibit increased epileptogenesis. **(A1)** Experimental paradigm used to assess seizure activity following the flurothyl kindling epileptogenesis model. **(A2)** Latency to myoclonic in wild-type ($Ecm29^{+/+}$; n = 15), Ecm29 heterozygous ($Ecm29^{+/-}$; n = 15), and Ecm29 null ($Ecm29^{-/-}$; n = 15) mice after flurothyl treatment (**, P < 0.01; ***, P < 0.001; ****, P < 0.0001 compared with wild-type group; multiple t tests). **(A3)** Changes in myoclonic seizure latency of the first (D1) and second (D2) flurothyl kindling traits indicate increased susceptibility of Ecm29 KO ($Ecm29^{-/-}$) mice. *, P < 0.05; ns, not significant by unpaired t test. **(A4)** Shorter latency from myoclonic to generalized seizure of the first kindling traits (Day 1) reveals a lower convulsive threshold in Ecm29 KO ($Ecm29^{-/-}$) mice (**, P < 0.01; ns, not significant by unpaired t test). **(A5)** Survival of Ecm29 homozygous KO mice was significantly lower than that of wild-type or Ecm29 heterozygotes over eight seizure traits. *, P < 0.05 based on log-rank test. **(A6)** Paradigm shown in top panel depicts time courses of daily DMSO (2% in 100 µl saline) or BUM (0.2 mg/kg body weight) administration at perinatal ages (from P7 to P14), followed by flurothyl exposure once daily for 8 d from P35 (red bars). Histograms of latency from myoclonic to generalized seizure of the first kindling traits (middle panel) and susceptibility index (bottom panel) show that daily BUM administration (0.2 mg/kg body weight) at perinatal ages (P7–P14) reduces severity of flurothyl-induced seizures in Ecm29 KO juvenile mice. Data points represent mean ± SEM; n = 11–15 animals per group; *, P < 0.05, two-way ANOVA followed by Tukey's multiple comparison test, comparing data to the $Ecm29^{+/+}$ group and corresponding DMSO (2% in 100 µl saline) control groups. **(B1)** Ecm29 homozygous KO mice ($Ecm29^{-/-}$) exhibit increased susceptibility to PTZ-induced seizures (60 mg/kg; i.p.) relative to wild-type mice. Hypoactivity (HYPO; phase 1); PC (phase 2); GC (phase 3); GTC (phase 4). Data points represent mean ± SEM; n = 20 animals per group; *, P < 0.05; **, P < 0.01, t test comparing data to the $Ecm29^{+/+}$ group. **(B2)** Higher number of MCs and GC/GTCs reveals greater seizure severity in Ecm29 KO ($Ecm29^{-/-}$) mice. Data points represent mean ± SEM; n = 20 animals per group; *, P < 0.05, t test comparing data to the $Ecm29^{+/+}$ group. **(B3)** 60 mg/kg was not the lethal dose for most test mice, based on log-rank test. **(C)** NKCC1 inhibition rescues $Ecm29^{-/-}$ juvenile mice from hypersensitivity to PTZ-induced convulsion. **(C1 and C2)** Paradigm shown in top panel depicts time courses of daily DMSO (2% in 100 µl saline) or BUM (0.2 mg/kg body weight) administration at perinatal ages (P7–P14, C1) or at late juvenile stages (P50–P57, C2), followed by 60 mg/kg PTZ i.p. challenge at P60 (red dot). Histograms of number of PC/GTC episodes (middle and bottom panels, C1) and susceptibility scores (middle and bottom panels, C2) show that BUM administration at P7 reduces severity of PTZ-induced seizures in Ecm29 KO mice. Data points represent mean ± SEM; n = 11–22 animals per group; *, P < 0.05; **, P < 0.01; ns, not significant by t test comparing data to the $Ecm29^{+/+}$ group and corresponding DMSO control groups.

Grubb and Burrone, 2010), we asked whether altered NKCC1 levels and hyperexcitability observed in immature Ecm29 KO neurons are sufficient to drive structural changes in AIS position or extent at early time points (5–14 DIV), a time period before maturation of conventional excitatory synapses. Since the pattern of AnkG staining in axons of young cortical neurons is represented by a bell-shaped curve, we defined positions of 50% peak AnkG intensity at either tail of the curve as AIS start and end positions. As in wild-type cortical neurons depicted in Fig. 7 A, the AIS start position at 5 DIV was located ~10 µm away from

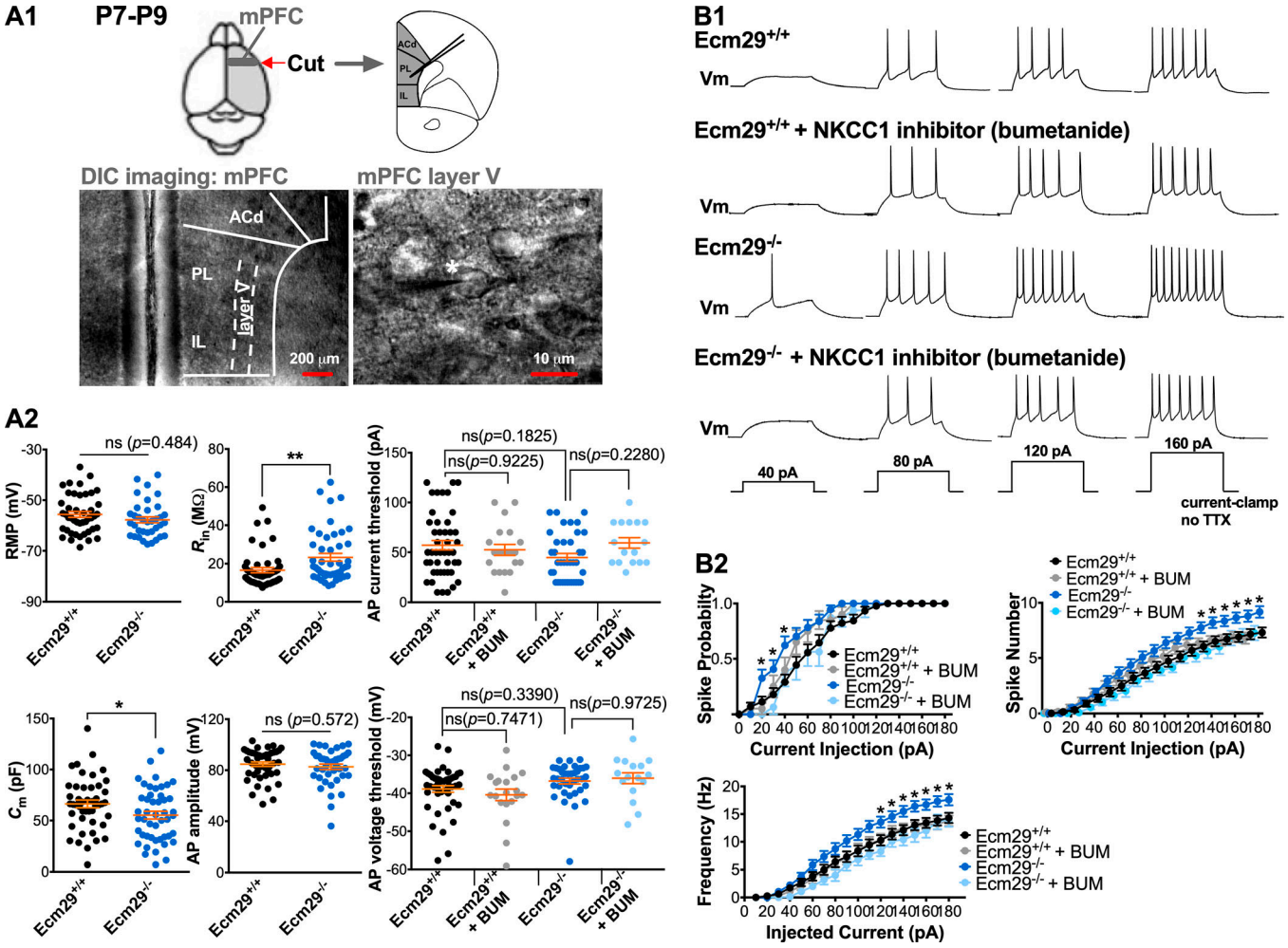

Figure 6. **NKCC1 blockade plus BUM treatment alleviates aberrant neuronal excitability in developing Ecm29 KO neurons. (A1)** Representative differential interference contrast (DIC) images of whole-cell patch clamp recordings of layer V pyramidal neurons in mPFC slices prepared from P7–P9 mice. ACd, dorsal anterior cingulated cortex; IL, infralimbic cortex; PL, prelimbic cortex. **(A2)** Graphs summarizing various intrinsic membrane properties of mPFC layer V neurons in wild-type (Ecm29$^{+/+}$) and Ecm29 KO (Ecm29$^{-/-}$) mice in the presence or absence of the NKCC1 inhibitor BUM (10 µM; ±SEM, n > 20 per group; *, P < 0.05; **, P < 0.01; ns, not significant by unpaired t test or two-way ANOVA followed by Tukey's multiple comparison test). C_m, membrane capacitance; R_{in}, input resistance. **(B1)** Representative traces of APs evoked by a 40-nA step current with or without 10 µM BUM application. **(B2)** Graphs show that mPFC layer V neurons of Ecm29 KO (Ecm29$^{-/-}$) mice exhibit hyperexcitability (as reflected by spike probability, number, and frequency) at different current steps, and that hyperexcitability is abolished by BUM application. Data (±SEM, n > 20 per group) obtained from the same sets of experiments shown in A2. *, P < 0.05 compared with wild-type group by multiple t tests.

the soma, gradually became closer (~2.5 µm) to the soma on 7 DIV, and was directly adjacent to the soma on 14 DIV. Such a shift may be a consequence of neurons becoming more excitable during this time window (Grubb et al., 2011). Indeed, we observed a significantly larger proximal shift (~5 µm) in AIS start position at 5 and 7 DIV in Ecm29 KO cortical neurons relative to comparably aged wild-type cortical neurons (Fig. 7 A). A similar abnormally accelerated proximal shift was seen in wild-type neurons following proteasome inhibition by either Rpt1 knockdown or treatment with MG132 or lactacystin for 8 h (Fig. 7 B). Notably, these treatments had no additional effects on AIS positional shifts in Ecm29 KO neurons, implying that proteasomes require Ecm29 expression to be functional. However, the accelerated proximal shift in AIS start position observed in 7-DIV Ecm29 KO cortical neurons was ameliorated following either ectopic expression of Ecm29 or NKCC1 inhibition with 10 µM BUM for 3 d (Fig. 7, A and B), suggesting that AIS structural dynamics are changed in response to altered excitability caused by elevated NKCC1 level/activity and Ecm29 loss. Finally, we observed comparable levels of voltage-gated sodium channels (Na_V), as detected by pan-Na_V antibodies, at the AIS in wild-type and Ecm29 KO cortical neurons at 7 DIV (Fig. 7 C). Overall, the results suggest that altered neuronal excitability caused by Ecm29 loss, proteasome dysfunction, and/or NKCC1 accumulation in immature neurons perturbs developmental AIS positioning (Fig. 7 D).

Discussion

Newly differentiated neurons are unique in their intrinsic tendency to undergo several rounds of activity and morphologic transformation before attaining a fully mature state and their

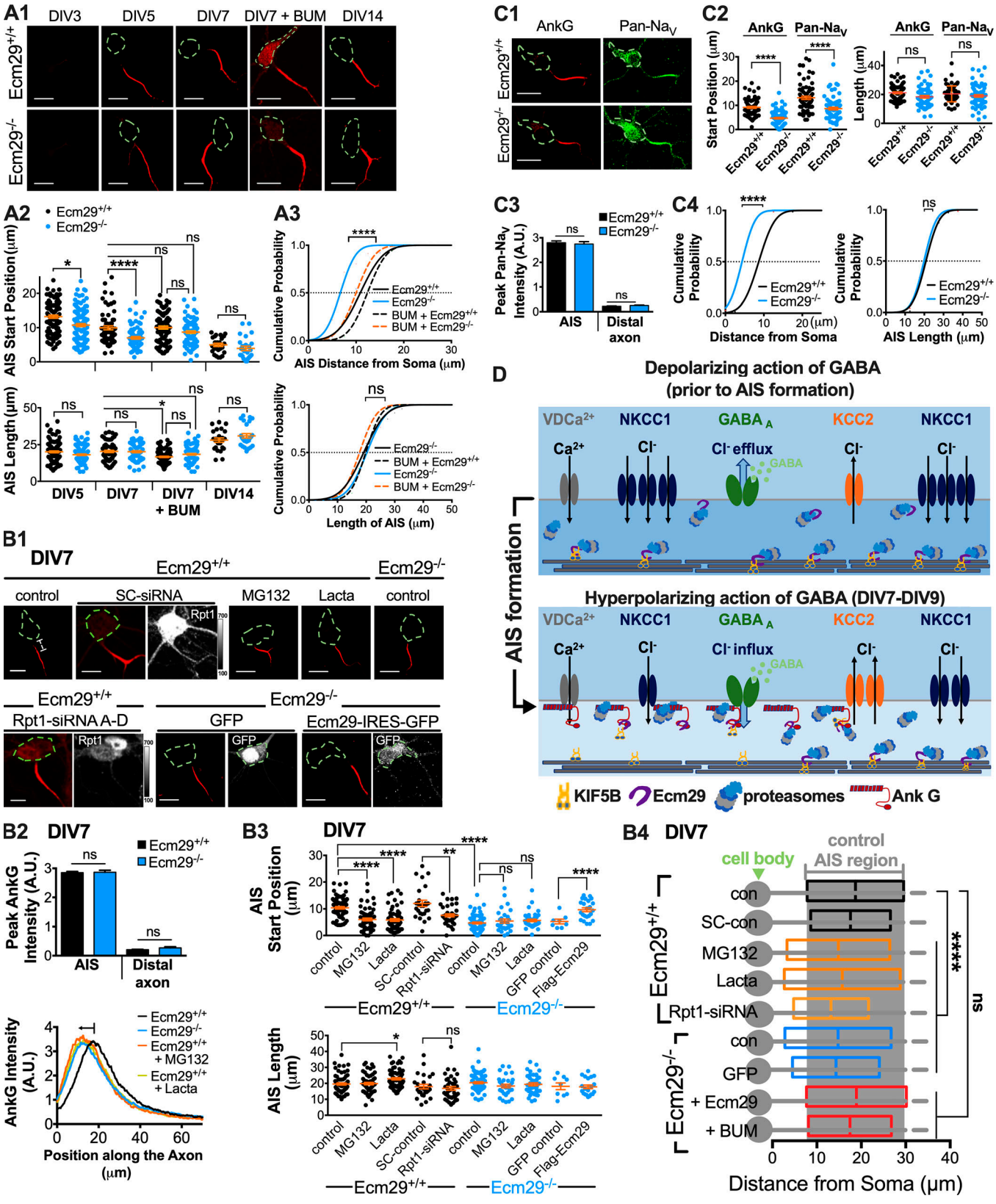

Figure 7. **Proteasome and NKCC1 activities modulate AIS dynamics via Ecm29. (A)** Ecm29 loss alters developmental AIS dynamics. **(A1)** Representative images of cortical neurons treated with or without 10 μM BUM and immunostained with AnkG antibodies at indicated time points. Scale bar, 20 μm. **(A2)** Scatter plot showing shorter distances from cell bodies of AIS start positions (upper panel) in Ecm29 KO ($Ecm29^{-/-}$) cortical neurons relative to wild-type ($Ecm29^{+/+}$) neurons in ∼5–7-DIV cultures. AIS start and end positions were estimated based on positions of 50% peak AnkG intensity at both tails, with the distance between these positions defining AIS length (lower panel). *, P < 0.05; ****, P < 0.0001, two-way ANOVA with Tukey's multiple comparisons post hoc

test. **(A3)** Cumulative probability plot showing that NKCC1 inhibition by 10 µM BUM treatment (+BUM; added at 4 DIV) restored the abnormally accelerated proximal shift in AIS position (upper panel) in 7-DIV Ecm29 KO neurons. Data from experiments similar to those described in A1 and A2. ****, P < 0.0001; ns, not significant, two-way ANOVA with Dunnett's post hoc test. **(B)** Blockade of proteasome activity causes an early proximal shift in AIS position in 7-DIV cortical neurons. **(B1)** Representative images of 7-DIV cortical neurons treated with or without proteasome inhibitors (MG132 or lactacystin; 2.5 µM, 8 h), and ectopically expressing SC-siRNA or Rpt1 targeting-siRNA (Rpt1-siRNA A-D), and/or control GFP or Ecm29-IRES-GFP, followed by immunostaining with AnkG antibodies (red) or Rpt1 antibody (gray). Scale bars, 20 µm. **(B2 and B3)** Averaged AnkG intensity along axons (n ≥ 57 per group; B2) and summary scatter plot (n = 7–68; B3) showing that proteasome inhibition and Ecm29 loss significantly shorten the AIS start position relative to that seen in wild-type neurons (±SEM; *, P < 0.05; **, P < 0.01; ****, P < 0.0001; ns, not significant, one-way ANOVA followed by Dunnett's post hoc test). Note that AIS integrity, as reflected by the peak AnkG intensity (upper panel, B2), is comparable in wild-type and Ecm29 KO neurons. **(B4)** Histogram (*n* = 7–68 per group; ****, P < 0.0001; ns, not significant, one-way ANOVA followed by Dunnett's post hoc test) showing effects of proteasome and NKCC1 inhibition on the changes in the AIS start position and length. **(C)** Similar to A, except that 7-DIV cortical neurons were costained with antibodies against pan-voltage-gated Na^+ channels (Pan-Na_V; C1–C3). Scale bar, 20 µm. Note that both pan-Na_V and AnkG start positions in Ecm29 KO neurons exhibit an accelerated proximal shift in AIS position (C2 and C4). Data represent mean ± SEM, *n* > 60 cells per group from three independent experiments. ****, P < 0.0001; ns, not significant by one-way ANOVA followed by Dunnett's post hoc test. **(D)** Schematic illustrating proposed AIS-associated, $Ecm29^{-/-}$ proteasome-dependent modulation of GABA-evoked excitability properties in maturing neurons, requiring developmental NKCC1 down-regulation and proper subcellular localization of proteasomes.

capacity to transduce information encoded by electrical and chemical signals. Here, we found that retention of Ecm29-associated proteasomes in the AIS region spatiotemporally fine-tunes chloride homeostasis, allowing timely transformation of maturing neurons from GABA excitable to GABA inhibitory. Dysregulation of proteasome distribution caused by Ecm29 loss led to an abnormal increase in NKCC1 abundance in both the somatodendritic compartment and the AIS region of maturing neurons, as well as a prolonged excitatory response to GABA, a phenotype rescued by either ectopic Ecm29 expression or pharmaceutical NKCC1 inhibition. NKCC1 inhibition at perinatal age (P7), before the GABA switch, was sufficient to alleviate hypersusceptibility to chemically induced seizures in Ecm29 KO mice. Together, we demonstrate that alteration of excitability properties in maturing neurons requires regulation of the subcellular localization of proteasomes.

Proteasome complexes in newly polarized hippocampal or cortical neurons acquire a microtubule-based active axonal/dendritic trafficking system that biases protein homeostasis in different compartments toward protein machineries favoring axonal growth (Hsu et al., 2015). Even so, the AIS in the proximal axon secures cell polarity (Debanne et al., 2011; Hedstrom et al., 2008; Rasband, 2010) and serves as a unique domain for ion channel clustering to facilitate AP firing (Araki and Otani, 1955; Coombs et al., 1957; Fuortes et al., 1957; Kole and Stuart, 2012). Little is known about whether and how proteasomal distribution and local protein turnover regulate structure/function properties of the AIS as GABAergic neurotransmission moves from excitatory to inhibitory. The current working model suggests that a developmental increase in KCC2 mRNA transcripts seen at the second postnatal week in mice lowers the $[Cl^-]_i$ (Kahle et al., 2013; Kaila et al., 2014; Leonzino et al., 2016; Medina et al., 2014), reversing the directionality of GABA-evoked chloride flux. Enhanced expression of the chloride exporter KCC2 renders neurons less excitable by shifting the voltage dependence of activation toward more positive potentials, causing sodium channels to open above resting potentials. Of note, the AIS membrane of cortical pyramidal neurons exerts a much more positive reversal potential of $GABA_A$ receptor–mediated current (toward more depolarized values) than does the somatodendritic compartment, and responses were mainly attributable to chloride uptake mediated by NKCC1, but not KCC2, around the AIS region (Khirug et al., 2008; Rinetti-Vargas et al., 2017). Our study reveals another tier of regulation, namely via Ecm29-mediated and AnkG-sorted proteasomal distribution to reduce NKCC1 protein levels spatiotemporally in developing neurons, before the first postnatal week. The preferential NKCC1 degradation of the AIS-located Ecm29/proteasome complexes could be a result of differential protein expression profiles during the GABAergic switch, which is concomitant with the decline of NKCC1 RNA transcripts and constitutes a time window when NKCC1 protein abundance and function predominate over other ion channels, such as KCC2, Na_v channels, Kainate, AMPA, and NMDA receptors. In this scenario, NKCC1 in the proximal axon may be a relatively accessible substrate (given its abundance) at the AIS for the proteasome relative to other ion channels; hence, a shift in the NKCC1 decline curve caused by proteasome dysregulation would become evident. Since Ecm29 is required to keep NKCC1 protein from spreading away from the AIS region of maturing cortical neurons, we hypothesized that Ecm29-associated proteasome activity and retention in the AIS prevents developing neurons from undergoing aberrant neuronal activation. Accordingly, we found that aberrant proteasome distribution following Ecm29 loss indeed led to a delay in the GABA polarity switch. Consequently, Ecm29 KO cortical neurons exhibited elevated intrinsic excitability, and mice lacking Ecm29 were vulnerable to chemically induced epilepsy, a phenotype frequently associated with AIS dysfunction and abnormal elevation of NKCC1 levels (Dzhala et al., 2010; Wang et al., 2017a; Wimmer et al., 2010a, 2010b).

Proper dynamics of the AIS region is not only critical to prime neuronal depolarization but to establish appropriate input/output connectivity within neural circuits (Muir and Kittler, 2014; Wefelmeyer et al., 2015). This latter property has been termed AIS structural plasticity (Grubb and Burrone, 2010; Grubb et al., 2011). Recent studies of mature pyramidal neurons found that chorionic depolarization led to distal shifts in the AIS position, while the positions of inhibitory GABAergic synapse, that is, axo-axonic connections in proximal axons, were not changed (Muir and Kittler, 2014; Wefelmeyer et al., 2015). The spatial mismatch between GABAergic synapses and the AIS could cause a higher shunting inhibition of GABAergic synapses that increases AP firing threshold and renders neurons less excitable (Baranauskas et al., 2013; Wefelmeyer et al., 2015). Our

study, which was performed at an earlier developmental time point before the GABA polarity switch, reports a different type of plastic AIS positioning in response to local protein homeostasis stresses and [Cl^-] dynamics. We observed a proximal shift of the AIS toward the cell body when young pyramidal neurons were still excitable by GABA, a developmental AIS positioning that was NKCC1 activity dependent. Conversely, altered NKCC1 accumulation in proximal axons caused by proteasome dysregulation would not only accelerate proximal AIS shifts but also perturb homeostatic regulation of GABAergic synapses and the AIS, leading to a hyperexcitable neuron (Gulledge and Bravo, 2016).

Damaged or mutant channel and/or structural proteins associated with the AIS are considered high-risk factors for neurodevelopmental and psychiatric disorders, including epilepsy, autism spectrum disorder, schizophrenia, and bipolar disorder (Buffington and Rasband, 2011; Hsu et al., 2014). Conversely, some neurodevelopmental or psychiatric disorders may be caused by altered local proteostasis at the AIS in early developmental stages. Our findings provide a developmental mechanism linking timing of AIS formation, proteasome transport, and subcellular proteostasis to the critical window of the GABAergic polarity switch, which governs excitability of maturing hippocampal/cortical neurons and is mediated by Ecm29. Moreover, results of behavioral tasks assessed in our Ecm29 KO mouse model support the idea that Ecm29 is necessary for normal juvenile social interactions and neuronal excitability, as reflected in a developmental shift in AIS position. Notably, although our findings have focused on the AIS, AnkG isoforms (190, 270, and 480 kD) are also found in dendrites and dendritic synapses, in which AnkG plays a role in GABAergic synapse maintenance and dendritic architecture regulation (Smith et al., 2014; Tseng et al., 2015). As such, the proteasome-associated function should also act on somatodendritic GABAergic synapses via similar Ecm29–AnkG association mechanisms, contributing a global, rather than an AIS-specific, homeostatic control on intracellular ion balance and neuronal modulation at perinatal and/or later stages.

Looking forward, our observations and model that integrates developmental changes in proteasome distribution with timing of AIS formation establish a synergistic mechanism that drives the GABAergic polarity switch underlying timely neuronal maturation and appropriate excitability. Apart from proteasome-mediated protein degradation, physiological protein turnover imposed by other reactions—such as receptor-mediated endocytosis, membrane lateral diffusion, trafficking, or calpain-mediated proteolysis—could play important roles in ion homeostasis in the local membrane microenvironment (Chamma et al., 2013; Heubl et al., 2017; Puskarjov et al., 2012; Vacher and Trimmer, 2012). In addition to the GABAergic polarity switch, Ecm29-associated proteasome distribution may also modulate strength and efficacy of synaptic connections at neuronal terminals, providing another mechanism by which neuronal development is spatiotemporally controlled.

Materials and methods

Plasmids, antibodies, and materials

Plasmids used were as follows. Ecm29 full-length and truncated variants were subcloned into pCDH-mCherry or EGFP-N1-mCherry plasmids by PCR-based methods to establish FRET reporters to assess Ecm29–AnkG interaction. EGFP-N2-190AnkG-GFP (plasmid 31059; Mohler et al., 2002), pEGFP-N1-NF-186-HA (plasmid 31061; Zhang et al., 1998), and pcDNA3–PalmPalm-ClopHensor (plasmid 25940; Arosio et al., 2010) were obtained from Addgene. FLAG-tagged full-length or truncated versions of Ecm29 expression plasmids were generous gifts from Dr. Carlos Gorbea (University of Utah School of Medicine, Salt Lake City, UT; Gorbea et al., 2004). AIS-targeted protein turnover reporter pAAV-hSyn-NavII-III–GFPu was generated by cloning a PCR product containing the coding sequence of the N-terminal NavII-III–tagged GFPu into pAAV-hSyn-EGFP (a gift from Bryan Roth, University of North Carolina at Chapel Hill, Chapel Hill, NC; Addgene plasmid 50465) using In-fusion HD cloning kit (Clontech). AnkG siRNA constructs (Accell SMARTpool Ank3 siRNAs), a mixture of four siRNAs (5′-CUGGCUUCCUUUACGUUUU-3′, 5′-CUAUGAAUUGUAGAAGUAU-3′, 5′-CGCUUAUUUAAAUGUCUUA-3′, and 5′-UCAUAAUUAAGGAUUUGUA-3′), proteasome subunit Rpt1 siRNA constructs (5′-UUGUUAACCUUGGAAUCGA-3′, 5′-GUCGUAUGCCAAAUUUAGU-3′, 5′-GCAAGAUGUACCAAGAUAA-3′, and 5′-GCGGAGAUUAGAAGCGUUU-3′), and a scrambled siRNA (Acell Non-targeting siRNA #1: 5′-UGGUUUACAUGUCGACUAA-3′) were purchased from Dharmacon. AnkG shRNA constructs consisted of three 29-oligonucleotide duplexes targeting rat AnkG (shRNA A targeting position 397, shRNA C targeting position 2,211, and shRNA D targeting position 5,759 of the corresponding AnkG coding sequence), and a control scrambled shRNA cassette cloned into pGFP-C-shLenti vector (OriGene Technologies). GST-tagged fusion protein expression constructs encoding full-length or truncated versions of AnkG or Ecm29 were generated by Gateway Technology (Invitrogen) based on manufacturer's protocols. All constructs were sequenced to verify sequence integrity.

Sources of antibodies, proteins, and chemicals are as follows. Polyclonal 480AnkG and Pan(SR)AnkG antibodies against the synthetic peptide corresponding to amino acids 3516–3530 and 1633–1650 of human AnkG, respectively, were custom-made by LTK BioLaboratories. Mouse monoclonal FLAG M2 (F1804) and pan-sodium channel (clone K58/35) antibodies were from Sigma-Aldrich. Polyclonal β III tubulin (AB9354), MAP2 (AB5622), α centractin Arp1 (Ab6058), and KCC2 (07-432) antibodies, and monoclonal actin (clone C4, MAB1501) and Tau-1 (clone PC1C6, MAB3420) antibodies were from Merck Millipore. Rabbit polyclonal ECM29 (ab28666), KIF5B (ab5629), and KLC (ab95882) antibodies, goat polyclonal antibody to DCTN1 (ab11806), and mouse monoclonal antibody to mCherry (ab125096) were from Abcam. Polyclonal antibody to ubiquitin (GTX19247) and monoclonal antibody to GADPH (clone GT239, GTX627408) were from GeneTex. Polyclonal antibody to 20S core subunits (BML-PW8815) and monoclonal antibody to Rpt1 (BML-PW8825) and Rpt5 (BML-PW8770) were from Enzo. Monoclonal antibody to GFP (11814460001) was from Roche. Rabbit polyclonal AnkG (clone H-215 for IF), neurofascin (H-105), and AnkB (clone H-300) antibodies, goat polyclonal NKCC1 (N-16) and TRIM46 (clone T-14) antibodies, and mouse monoclonal AnkG (clone 463) and AnkB (clone 2.20) antibodies were

from Santa Cruz Biotechnology. Monoclonal AnkG (N106/20 and N106/36), pan-neurofascin (clone A12/18 and L11A/41), β4-spectrin (clone N393/76), Caspr (K65/35), Cav3.1 (N178A/9), and Cav3.2 (N55/10) antibodies were from the University of California, Davis/National Institutes of Health NeuroMab facility. Polyclonal Gephyrin (147 002 for Western blotting), GABA A receptor α2 (224 102 for Western blotting), GluN 2A/B (244 003), AMPA receptor GluA2 (182 103) antibodies and monoclonal Gephyrin (147 111 for IF), GABA A receptor α1 (224 211), GABA A receptor α2 (224 111 for IF), GABA A receptor γ2 (224 011), NMDA-Receptor/GluN1 (114 011), AMPA receptor GluA1 (182 011), and Neuroligin 2 (129 203) antibodies were from Synaptic Systems. Monoclonal antibody to NKCC1 (clone T4) was from Developmental Studies Hybridoma Bank. Monoclonal antibody to pan-sodium channel (clone K58/35) was from Sigma-Aldrich. Secondary antibodies were purchased from Life Technologies (Thermo Fisher Scientific) or Abcam. MV 151 was a generous gift from Dr. Herman S. Overkleeft (Leiden University, Leiden, Netherlands). Forskolin and KT5720 were from Calbiochem. BUM was purchased from Tocris Bioscience. MG132 (474790) was purchased from Merck Millipore, and clasto-Lactacystin β-lactone (70988) was from Cayman. Latrunculin A was from Santa Cruz Biotechnology. Nocodazole and PTZ were from Sigma-Aldrich. Suc-Leu-Leu-Val-Tyr-AMC (Suc-LLVY-AMC) was from Enzo. Bis(2,2,2-trifluoroethyl) ether was from TCI.

RNA extraction and quantitative RT-PCR analysis

Total RNA extraction from mouse brain tissue samples was performed using Tripure IsolationReagent (Roche) following the instruction manual. 1 µg of total RNA was reverse-transcripted into cDNA by using SuperScript III Reverse transcription (Invitrogen). Real-time signal detection and quantitative measurements of cDNA samples were performed by using the Fast SYBR Green Master Mix kit (Invitrogen) on the LightCycler 480 System (Roche). Primer sets specific for NKCC1, KCC2, or GAPDH are as follows: NKCC1 forward: 5′-GATTCGCAGAGACTGTGGTGGA-3′ and reverse: 5′-CTCCATTCCAGCCACTGAGATG-3′; KCC2 forward: 5′-GGGCAGAGAGTACGATGGC-3′ and reverse: 5′-TGGGGTAGGTTGGTGTAGTTG-3′; and GAPDH forward: 5′-AGGTCGGTGTGAACGGATTTG-3′ and reverse: 5′-TGTAGACCATGTAGTTGAGGTCA-3′.

Generation of Ecm29-deficient mice

All animal procedures were performed according to protocols approved by the Academia Sinica Institutional Animal Care & Utilization Committee. All mice were on a C57B/L6 genetic background. Ecm29-deficient mice were created by a CRISPR/Cas9 approach (gRNA sequence: 5′-CGCTTCTTACTGCCATGGAAGGG-3′), resulting in a guanine (G) deletion in *Ecpas* (*ECM29*) exon 4 (5′-ACTGCCATGGAAGGGAAA-3′ → 5′-ACTGCCAT–GAAGGGAAA-3′). A T7E1 assay and sequencing were employed to validate CRISPR edits, and no off-target mutations were detected. Heterozygous mice were backcrossed for >10 generations on a C57BL/6 J background. *ECM29* homozygous mice (*Ecm29*$^{-/-}$) and wild-type control littermates were obtained by heterozygous intercrossing.

Cell culture, protein lysate preparation, and immunostaining

Hippocampal neurons were prepared from rat embryos at E18 as described (Dotti et al., 1988) and cultured in neurobasal medium supplemented with Gem21 NeuroPlex (Gemini Bio-Products). A similar procedure was applied to prepare cortical neuronal cultures. HEK293T and Neuro2a cells were cultured in DMEM supplemented with 10% FBS (Biological Industries). Transfection was performed using a lentivirus-based expression system or Lipofectamine 2000 (Invitrogen) according to the manufacturer's instructions. Unless otherwise stated, hippocampal and cortical neurons were used as a standard model for in vitro immunocytochemistry to analyze neuronal morphology. Cortical neuronal cultures were used to obtain a sufficient number of cells for biochemical assays.

For cortical neuronal cultures, we prepared protein lysates in radioimmunoprecipitation assay buffer (Sigma-Aldrich) containing a complete protease inhibitor cocktail (Roche) and the phosphate inhibitor PhosSTOP (Roche). For tissue lysate preparation, brain was dissected from rat E17 embryos and rinsed briefly with PBS, followed by homogenization with a pestle in ice-cold lysis buffer (20 mM Tris-HCl, 5 mM $MgCl_2$, and 1 mM DTT) and followed by four cycles of sonication (20 s on followed by 10 s rest). For other biochemical experiments, cell lysates were prepared by the freeze-thaw method.

For immunostaining, cultured hippocampal or cortical neurons were fixed for 12 min in 4% PFA, permeabilized for 12 min in 0.3% Triton X-100, and blocked with 3% BSA for 1–2 h. Fixed cells were processed further for immunostaining according to standard procedures and imaged with a confocal microscope (Zeiss LSM700) equipped with a 63× oil-immersion objective (NA 1.4; Zeiss) and a 40× water-immersion objective (NA 1.1; Zeiss). For quantitative measurement of colocalization, we acquired images using SIM (Zeiss ELYRA PS1) equipped with a Plan Apo 63× oil-immersion objective (NA 1.4), and raw images were acquired with a total magnification of 79 nm per cameral pixel and z spacing of 125 nm between planes. Images were analyzed and processed using Zen software (Zeiss) and Imaris software (Bitplane). Surface rendering of the 3D images was performed using Zen and Imaris without z-correction. Images were analyzed and processed for presentation in figures using brightness and contrast adjustments with ImageJ software (National Institutes of Health) and following guidelines of Rossner and Yamada (Rossner and Yamada, 2004). For fluorescence intensity profiles shown in Fig. 1, A and B, intensity values were subtracted by the value at the distal axon (i.e., a data point taken 100 µm away from the cell body), and then converted to arbitrary units. To calculate intensity relative to the distal axon value shown in Fig. 1 E, the average intensity of the AIS region (AIS start and end positions were defined as positions of 50% of peak AnkG intensity values at either tail of the curve) was normalized to that of the distal axon (a 20-µm segment between data points at 60 and 80 µm).

OGD experiments were performed as described, with minor modifications (Schafer et al., 2009). In brief, hippocampal or cortical cultures at 7 DIV were incubated in glucose-free, deoxygenated balanced salt solution (BSS_0) containing 116 mM NaCl, 5.4 mM KCl, 0.8 mM $MgSO_4$, 1 mM NaH_2PO_4, 26.2 mM $NaHCO_3$,

1.8 mM $CaCl_2$, 0.01 mM glycine, 2 mM Glutamax, and 1× MEM amino acids (Invitrogen) and subjected to anaerobic conditions (5% CO_2, 95% N_2 [<0.2% O_2] at 37°C) for up to 30 min. For control groups, 7-DIV cultures were incubated in 20 mM glucose-containing solution (BSS_{20}) under normoxic conditions (5% CO_2, 95% air at 37°C) for up to 30 min. Cultures were returned to regular neuronal culture media for another 24 h before immunofluorescent staining.

Live-cell imaging of MV151-labeled proteasome subunits

Fluorescent labeling of proteasomes was performed as described (Verdoes et al., 2006). For live-cell imaging of proteasome transport across the AIS region, we preincubated neurons with pan-neurofascin antibody (A12/18) for 30 min to label the neurofascin extracellular domain that enabled us to detect the AIS, followed by 1-h incubation with proteasome-labeling agent MV151 (100 µM) and anti-mouse secondary antibody Alexa Fluor 488 conjugate (ab150113, Abcam) at 37°C in culture medium. Neurons were then visualized with a 6× oil-immersion objective (NA 1.4; Zeiss) in extracellular buffer (145 mM NaCl, 10 mM Hepes, 8 mM glucose, 3 mM $CaCl_2$, 2 mM $MgCl_2$, and 3 mM KCl) on a Zeiss Observer.Z1 microscope integrated with an AxioCam MRm camera and temperature/CO_2 modules. Zen blue software (Zeiss) was used for microscope control and data acquisition (0.5 Hz for 3 min, 90 frames total). MV151 was excited at λ_{ex} = 543 nm and detected at 560–620 nm.

Membrane-bound, AnkG-associated FRET imaging and analysis

HEK293 cells were cotransfected with plasmids encoding NF-186, 190AnkG-GFP, and Ecm29Δ-mCherry. Cells were imaged with a Rolera EM-C^2 EMCCD camera (QImaging) and Yokogawa CSU-X1 spinning-disk confocal microscopy (Zeiss) and a 40× water-immersion objective (NA 1.1; Zeiss). Excitation spectra were excited by a solid-state 488-nm diode laser, through a 517-nm dichroic filter. Emission spectra were sequentially acquired using 525 ± 30 nm and 605 ± 20 nm bandpass emission filters for GFP and mCherry fluorescence, respectively. Images were collected and analyzed with ImageJ. All filters and dichroics were from Chroma Technology. Live images were acquired for 9 min at 1.8-s intervals. Because the transmembrane protein NF-186 tethers associated complexes to the plasma membrane of the AIS region (Zhang and Bennett, 1998), measurements performed along the symmetric axis of the cell reveal a peripheral pattern indicative of AIS-associated localization. GFP and mCherry fluorescence intensities were measured at subsaturation levels for all pixels. For ratiometric FRET analysis, GFP and mCherry signals were background-subtracted (with background intensity taken from a proximal cell-free region) and normalized to a control value (averaged over the first 3 min of each experimental group), and the FRET value was calculated as a ratio (mCherry/GFP). FRET signal intensity was calculated with ImageJ and is represented by pseudocolors.

Expression of GST- and His-tagged proteins and in vitro binding assays

GST fusion proteins were produced as previously described. Briefly, we expressed GST- or His-tagged proteins in *Escherichia coli* BL21(DE3) induced by 0.4 mM IPTG overnight at 30°C in lysogeny broth medium. Bacteria were lysed by sonication in short pulses of 15 s in lysis buffer (50 mM Tris-HCl, pH 7.4, 50 mM NaCl, 5 mM DTT, 1 mM PMSF, and 1% Triton X-100 containing 1% Triton X-100, 1 mM EDTA, 1 mM DTT, and protease inhibitors [Complete EDTA-free; Roche]). Cell debris was removed by centrifugation at 9,000 *g* for 10 min at 4°C. Resultant supernatants were applied to Glutathione Sepharose 4B or HisTrap columns (GE Healthcare). After washing, GST- and His-tagged proteins were eluted in buffer containing 10 mM reduced glutathione or 300 mM imidazole, respectively. We added 1 M imidazole to samples shortly after elution to prevent precipitation of His-tagged protein. Protein concentration was measured using the Bio-Rad DC Protein Assay. Protein purity was further assessed by fast protein liquid chromatography, followed by SDS-PAGE and Coomassie blue staining.

For GST pull-down assays, we incubated cell lysate/His-tagged protein and GST fusion proteins together with glutathione-agarose beads. Complexes recovered from beads were resolved by SDS-PAGE and analyzed by Western blotting.

Membrane protein extraction from perinatal mouse cortex

Mouse brains at P0 and P14 were collected and immediately chilled in ice-cold oxygenated artificial cerebral spinal fluid (aCSF) containing 125 mM NaCl, 2.5 mM KCl, 1.2 mM NaH_2PO_4, 1.2 mM $MgCl_2$, 2.4 mM $CaCl_2$, 26 mM $NaHCO_3$, and 11 mM glucose, bubbled with 95% O_2/5% CO_2. Thick coronal sections of 300 µm were obtained with a vibratome (Leica VT1200S) and were recovered in aCSF at 31°C with gentle, continuous bubbling for 40 min. The recovered slices were then subjected to tissue surface protein biotinylation with 1.0 mg/ml EZ-Link Sulfo-NHS-SS-Biotin (Thermo Fisher Scientific) in chilled aCSF at 4°C for 45 min, bubbled with 95% O_2/5% CO_2. After washing three times with ice-cold aCSF and 10-min incubation in ice-cold aCSF on ice, the residual reactive biotin in slices was quenched twice with quenching buffer (ice-cold aCSF supplemented with 100 mM glycine) for 25 min on ice. Slices were washed three times with ice-cold aCSF, and then harvested by centrifugation at 200 *g* for 1 min at 4°C. The tissue pellet was homogenized and lysed in ice-cold radioimmunoprecipitation assay lysis buffer (Sigma-Aldrich) containing a complete protease inhibitor cocktail (Roche) and the phosphate inhibitor PhosSTOP (Roche), rotated for 30 min at 4°C. The tissue lysates were centrifugated at 18,000 *g* for 20 min at 4°C. Biotinylated proteins were purified from crude supernatant protein extracts by Pierce NeutrAvidin Agarose (Thermo Fisher Scientific) and subjected to Western blot analysis.

Fluorescence imaging and analysis of GABA-induced chloride fluxes

Cultured hippocampal and cortical neurons were transfected with plasmids encoding PalmPalm-ClopHensor using Lipofectamine 2000 (Invitrogen) at 4 DIV and imaged with an Evolve512 EMCCD camera (Photometrics) and Axio Observer Z1 microscopy (Zeiss) equipped with a 40× water-immersion objective (NA 1.1; Zeiss) at various time points as indicated in the figures. Excitation spectra for cyan, green, and DsRed fluorescence were

excited by solid-state 445-, 488-, and 561-nm total internal reflection fluorescence lasers, respectively. Typical measured power at the focal plane of the 40× objective (NA 1.1; Zeiss) was 0.8, 0.34, and 0.34 mW for laser lines at 445, 488, and 561 nm, respectively. Emission spectra were sequentially acquired using (445/525, BS; ET480/40m [465–490 nm], emission), (405/488/561/640, BS; ET525/50 [500–540 nm], emission), and (405/488/561/640, BS; ET595/44m [582–636 nm], emission) band-split and bandpass emission filters for the cyan channel (445-nm excitation), green channel (488-nm excitation), and DsRed channel (543-nm excitation) fluorescence, respectively. All filters and dichroics were from Chroma Technology. Images were acquired and collected with Zen Blue (Zeiss) and analyzed with ImageJ. Live images of each channel were acquired with an exposure of 150 ms, at 3-s intervals, over a total of 120 duty cycles. GABA (0.2 mM) was focally applied to the medium at the 40th iteration. All pixel intensities were measured at subsaturation levels, including those at processes and the soma. For analysis, PalmPalm-ClopHensor signals from the cyan, GFP, and DsRed channels were background-subtracted (with background intensity taken from a proximal cell-free region) and normalized by the basal value (from the first half-minute). All media and reagents were measured and adjusted to a final pH of 7.2–7.4. Changes in $[Cl^-]_i$ before and after focal GABA application were calculated and denoted by R_{Cl-}.

Fluo-4 calcium imaging

Hippocampal neurons were transferred to extracellular solution (145 mM NaCl, 10 mM Hepes, 8 mM glucose, 3 mM $CaCl_2$, 2 mM $MgCl_2$, and 3 mM KCl) before loading with the fluorescent Fluo-4 NW calcium indicator (Invitrogen). Time-lapse images of neurons loaded with 20 µM Fluo-4 NW were acquired at 400-ms intervals for 4.5 min (GABA was focally applied using a picospritzer from a glass pipette at 1.5-min time points) using Yokogawa CSU-X1 spinning-disk confocal microscopy (Zeiss). Image analysis of Fluo-4 dye intensity of the region of interest in cell bodies was performed using ImageJ. Pictures were taken with equal exposure in control and experimental groups.

Patch-clamp recording

Neonatal mice (P7–P9) were deeply anesthetized with isoflurane before immediate decapitation. We prepared 300-µm slices from mPFC in brain slicing/recording aCSF buffer (119 mM NaCl, 2.5 mM KCl, 1.3 mM $MgSO_4$, 1 mM NaH_2PO_4, 26.2 mM $NaHCO_3$, and 11 mM glucose, saturated with 95% O_2 and 5% CO_2). Recordings were performed for up to 4 h after slicing. Patch-clamp recordings were performed from the soma of layer V pyramidal neurons of the mPFC at 20–24°C in recording aCSF buffer. Recordings in voltage-clamp mode were performed using patch-clamp amplifiers (Axon multiclamp 700 B microelectrode amplifier; Molecular Devices). Signals were low-pass filtered at 1 kHz and sampled at 20 kHz using Clampex software (pClamp suite v10.5; Molecular Devices). Series resistance was compensated at 80% (lag 30–60 µs) before break-in. Micropipettes were made from borosilicate glass capillaries (G150F-4; Warner Instruments) with a resistance of 3–4 MΩ. The intracellular solution contained 131 mM K-gluconate, 20 mM KCl, 10 mM Hepes, 2 mM EGTA, 8 mM NaCl, 2 mM Mg-ATP, 0.3 mM Na-GTP, and 6.7 mM biocytin, pH 7.2, and osmolarity was adjusted to 300–310 mOsmol. The RMP was measured immediately after break-in and upon establishing whole-cell recording. Input resistance (R_{in}) was calculated by the slope of the linear portion of the current–voltage relationship obtained by measuring changes in steady-state potential in response to steps of increasing intensity of hyperpolarizing current (from −20 to +180 pA, 10-pA increments, 500-ms duration) using Clampfit (pClamp suite version 10.5; Molecular Devices). APs were isolated offline and identified as fast voltage transients that crossed a threshold value of 10 mV. The threshold for firing was determined by measuring voltage at the upward deflection of the trace. All measures were performed using CED Signal software (version 4.08, Cambridge Electronic Design).

Paradigms to assess chemical-induced seizure

Flurothyl-induced seizure experiments were performed as reported (Judson et al., 2016). Test mice were placed individually within a large (capacity 1,800 ml) crystallizing dish with a lid in a ventilated chemical hood for 2 min of habituation before flurothyl exposure (10% flurothyl in ethanol). Flurothyl was infused onto a gauze pad via a 3-ml syringe at a flow rate of 200 µl/min. Testing sessions were recorded and seizure onset was scored offline by an experimenter blind to genotype. Patterns of flurothyl-induced seizure per episode were analyzed as follows: (1) latency to the first myoclonic jerk (i.e., brief, but severe, contractions of neck and body musculature as the mouse maintained postural control); and (2) latency to the first generalized seizure (convulsions resulting in loss of postural control). Following a generalized seizure, the lid of the chamber was immediately removed, exposing the mouse to fresh air and facilitating seizure cessation. The chamber was cleared with 70% ethanol, and the gauze pad was replaced between trials.

For the PTZ-induced seizure model, we administered saline or PTZ (at doses of 50, 60, or 70 mg/kg) i.p. once a day and immediately videotaped the test animal in a chamber (30 cm length × 30 cm width × 30 cm height). Seizures were scored according to the following modified Racine scale (Ferraro et al., 1999; Naydenov et al., 2014) designed for mouse PTZ-induced seizures. Phase 1, hypoactivity, is characterized by progressive decrease in motor activity until the animal rests in a crouched or prone position with its abdomen in full contact with the cage base. Phase 2, partial clonus or myoclonic seizure (PC or MC), is clonic seizure activity affecting the face, head, and/or forelimbs. Partial or focal seizures are brief, typically lasting 1 or 2 s, and often accompanied by vocalizations; partial seizures occur either individually or in multiple discrete episodes before generalized seizure (see phase 3). Phase 3, GC, is characterized by the tail held straight up stiffly. Phase 4, generalized tonic-clonic (GTC), is a generalized seizure characterized by tonic hind limb extension or sudden loss of upright posture. Whole-body clonus involves all four limbs and tail, rearing events, and autonomic signs. Phase 4 also includes erratic running and jumping, which typically signals onset of a maximal seizure. Duration of generalized seizures typically involves behavioral changes lasting 30–60 s followed by a quiescent period. Most mice exhibit

multiple generalized seizures, irrespective of subsequent status for tonic hindlimb extension.

The seizure susceptibility score was calculated according to the following formula:

$$\left[\begin{array}{l}(0.2 \times 1/\text{PC latency}) + (0.3 \times 1/\text{GC latency}) + \\ (0.5 \times 1/\text{GTC latency})\end{array}\right] \times \sqrt{(\text{PC} + \text{GTC episode})}.$$

Note that optimal PTZ doses were determined from dose-response assessment. PTZ administration at 50 mg/kg i.p. was ineffective to induce GC. 70 mg/kg caused very rapid generation of GC/GTC, and most test mice died before the end of the 30-min session. Therefore, here, PTZ-induced seizures were elicited using a dose of 60 mg/kg i.p.

Statistical analysis

To select the appropriate statistical test for comparing two datasets, we first determined whether each dataset was normally distributed using a Jarque–Bera test. For datasets with normal distributions, *t* tests were used. For comparisons involving multiple datasets, ANOVA followed by a post hoc Dunnett's or Tukey's test was employed.

Online supplemental material

Fig. S1 (related to Fig. 1) shows AnkG down-regulation but no neuritic/axonal beading in neurons after 30-min OGD. Fig. S2 (related to Fig. 2) supports the finding that the Ecm29 N-terminal associates with the AnkG C-terminal. Figs. S3 and S4 (related to Figs. 3, 4, and 5) show protein expression profiles or subcellular distributions of proteins associated with GABA transmission in wild-type and Ecm29 KO cortical lysates or 7-DIV neurons. Fig. S5 (related to Fig. 4 E) indicates that GABA-induced Ca^{2+} transients are dependent on activation of L-type calcium channels. Video 1 (related to Figs. 1 C and 2) shows transport behavior of MV151-labeled proteasomes in wild-type and Ecm29 KO cortical neurons. Video 2 (related to Fig. 5) shows spontaneous onset of absence seizures/partial seizures observed in an Ecm29 KO mouse in a home-cage environment.

Acknowledgments

We thank Hwai-Jong Cheng for discussions and critical reading of the manuscript. We thank the IMB Transgenic Core Facility (Institute of Molecular Biology, Academia Sinica) for help with Ecm29 KO mice generation. We thank the IMB Genomics Core Facilities (Institute of Molecular Biology, Academia Sinica) for quantitative RT-PCR analysis.

This work was supported in part by the Ministry of Science and Technology, Taiwan (grant 106-2311-B-001-017-MY3).

The authors declare no competing financial interests.

Author contributions: M. Lee conceptualized, performed, analyzed, and validated biochemistry experiments, IF staining, plasmid construction, quantitative RT-PCR, and the FRET assay, and cowrote the manuscript. Y.-C. Liu, C. Chen, and S.-T. Lu performed and analyzed biochemistry experiments. C.-H. Lu and T.-N. Huang supervised, performed, and analyzed animal behavior assays. M.-T. Hsu performed and analyzed proteasome transport assays. Y.-P. Hsueh supervised animal behavior assays. P.-L. Cheng supervised, conceptualized, performed, and analyzed live cell imaging and IF staining and cowrote the manuscript. All authors read and contributed to the manuscript.

Submitted: 6 March 2019
Revised: 14 October 2019
Accepted: 13 November 2019

References

Alvarez-Leefmans, F.J., S.M. Gamiño, F. Giraldez, and I. Noguerón. 1988. Intracellular chloride regulation in amphibian dorsal root ganglion neurones studied with ion-selective microelectrodes. *J. Physiol.* 406: 225–246. https://doi.org/10.1113/jphysiol.1988.sp017378

Amin, H., F. Marinaro, D. De Pietri Tonelli, and L. Berdondini. 2017. Developmental excitatory-to-inhibitory GABA-polarity switch is disrupted in 22q11.2 deletion syndrome: a potential target for clinical therapeutics. *Sci. Rep.* 7:15752. https://doi.org/10.1038/s41598-017-15793-9

Araki, T., and T. Otani. 1955. Response of single motoneurons to direct stimulation in toad's spinal cord. *J. Neurophysiol.* 18:472–485. https://doi.org/10.1152/jn.1955.18.5.472

Arosio, D., G. Garau, F. Ricci, L. Marchetti, R. Bizzarri, R. Nifosì, and F. Beltram. 2007. Spectroscopic and structural study of proton and halide ion cooperative binding to gfp. *Biophys. J.* 93:232–244. https://doi.org/10.1529/biophysj.106.102319

Arosio, D., F. Ricci, L. Marchetti, R. Gualdani, L. Albertazzi, and F. Beltram. 2010. Simultaneous intracellular chloride and pH measurements using a GFP-based sensor. *Nat. Methods.* 7:516–518. https://doi.org/10.1038/nmeth.1471

Báldi, R., C. Varga, and G. Tamás. 2010. Differential distribution of KCC2 along the axo-somato-dendritic axis of hippocampal principal cells. *Eur. J. Neurosci.* 32:1319–1325. https://doi.org/10.1111/j.1460-9568.2010.07361.x

Banke, T.G., and C.J. McBain. 2006. GABAergic input onto CA3 hippocampal interneurons remains shunting throughout development. *J. Neurosci.* 26:11720–11725. https://doi.org/10.1523/JNEUROSCI.2887-06.2006

Baranauskas, G., Y. David, and I.A. Fleidervish. 2013. Spatial mismatch between the Na+ flux and spike initiation in axon initial segment. *Proc. Natl. Acad. Sci. USA.* 110:4051–4056. https://doi.org/10.1073/pnas.1215125110

Barry, J., Y. Gu, P. Jukkola, B. O'Neill, H. Gu, P.J. Mohler, K.T. Rajamani, and C. Gu. 2014. Ankyrin-G directly binds to kinesin-1 to transport voltage-gated Na+ channels into axons. *Dev. Cell.* 28:117–131. https://doi.org/10.1016/j.devcel.2013.11.023

Ben-Ari, Y. 2002. Excitatory actions of gaba during development: the nature of the nurture. *Nat. Rev. Neurosci.* 3:728–739. https://doi.org/10.1038/nrn920

Ben-Ari, Y., E. Cherubini, R. Corradetti, and J.L. Gaiarsa. 1989. Giant synaptic potentials in immature rat CA3 hippocampal neurones. *J. Physiol.* 416: 303–325. https://doi.org/10.1113/jphysiol.1989.sp017762

Bence, N.F., E.J. Bennett, and R.R. Kopito. 2005. Application and analysis of the GFPu family of ubiquitin-proteasome system reporters. *Methods Enzymol.* 399:481–490. https://doi.org/10.1016/S0076-6879(05)99033-2

Berger, S.L., A. Leo-Macias, S. Yuen, L. Khatri, S. Pfennig, Y. Zhang, E. Agullo-Pascual, G. Caillol, M.S. Zhu, E. Rothenberg, et al. 2018. Localized Myosin II Activity Regulates Assembly and Plasticity of the Axon Initial Segment. *Neuron.* 97:555–570.e6. https://doi.org/10.1016/j.neuron.2017.12.039

Buffington, S.A., and M.N. Rasband. 2011. The axon initial segment in nervous system disease and injury. *Eur. J. Neurosci.* 34:1609–1619. https://doi.org/10.1111/j.1460-9568.2011.07875.x

Cellot, G., and E. Cherubini. 2014. GABAergic signaling as therapeutic target for autism spectrum disorders. *Front Pediatr.* 2:70. https://doi.org/10.3389/fped.2014.00070

Chamma, I., M. Heubl, Q. Chevy, M. Renner, I. Moutkine, E. Eugène, J.C. Poncer, and S. Lévi. 2013. Activity-dependent regulation of the K/Cl transporter KCC2 membrane diffusion, clustering, and function in hippocampal neurons. *J. Neurosci.* 33:15488–15503. https://doi.org/10.1523/JNEUROSCI.5889-12.2013

Côme, E., M. Heubl, E.J. Schwartz, J.C. Poncer, and S. Lévi. 2019. Reciprocal Regulation of KCC2 Trafficking and Synaptic Activity. *Front. Cell. Neurosci.* 13:48. https://doi.org/10.3389/fncel.2019.00048

Coombs, J.S., D.R. Curtis, and J.C. Eccles. 1957. The interpretation of spike potentials of motoneurones. *J. Physiol.* 139:198–231. https://doi.org/10.1113/jphysiol.1957.sp005887

De La Mota-Peynado, A., S.Y. Lee, B.M. Pierce, P. Wani, C.R. Singh, and J. Roelofs. 2013. The proteasome-associated protein Ecm29 inhibits proteasomal ATPase activity and in vivo protein degradation by the proteasome. *J. Biol. Chem.* 288:29467–29481. https://doi.org/10.1074/jbc.M113.491662

Debanne, D., E. Campanac, A. Bialowas, E. Carlier, and G. Alcaraz. 2011. Axon physiology. *Physiol. Rev.* 91:555–602. https://doi.org/10.1152/physrev.00048.2009

Dotti, C.G., C.A. Sullivan, and G.A. Banker. 1988. The establishment of polarity by hippocampal neurons in culture. *J. Neurosci.* 8:1454–1468. https://doi.org/10.1523/JNEUROSCI.08-04-01454.1988

Dumitrescu, A.S., M.D. Evans, and M.S. Grubb. 2016. Evaluating Tools for Live Imaging of Structural Plasticity at the Axon Initial Segment. *Front. Cell. Neurosci.* 10:268. https://doi.org/10.3389/fncel.2016.00268

Dzhala, V.I., K.V. Kuchibhotla, J.C. Glykys, K.T. Kahle, W.B. Swiercz, G. Feng, T. Kuner, G.J. Augustine, B.J. Bacskai, and K.J. Staley. 2010. Progressive NKCC1-dependent neuronal chloride accumulation during neonatal seizures. *J. Neurosci.* 30:11745–11761. https://doi.org/10.1523/JNEUROSCI.1769-10.2010

Ferraro, T.N., G.T. Golden, G.G. Smith, P. St Jean, N.J. Schork, N. Mulholland, C. Ballas, J. Schill, R.J. Buono, and W.H. Berrettini. 1999. Mapping loci for pentylenetetrazol-induced seizure susceptibility in mice. *J. Neurosci.* 19:6733–6739. https://doi.org/10.1523/JNEUROSCI.19-16-06733.1999

Fujioka, T., A. Fujioka, and R.S. Duman. 2004. Activation of cAMP signaling facilitates the morphological maturation of newborn neurons in adult hippocampus. *J. Neurosci.* 24:319–328. https://doi.org/10.1523/JNEUROSCI.1065.03.2004

Fuortes, M.G., K. Frank, and M.C. Becker. 1957. Steps in the production of motoneuron spikes. *J. Gen. Physiol.* 40:735–752. https://doi.org/10.1085/jgp.40.5.735

Galiano, M.R., S. Jha, T.S. Ho, C. Zhang, Y. Ogawa, K.J. Chang, M.C. Stankewich, P.J. Mohler, and M.N. Rasband. 2012. A distal axonal cytoskeleton forms an intra-axonal boundary that controls axon initial segment assembly. *Cell.* 149:1125–1139. https://doi.org/10.1016/j.cell.2012.03.039

Ganguly, K., A.F. Schinder, S.T. Wong, and M. Poo. 2001. GABA itself promotes the developmental switch of neuronal GABAergic responses from excitation to inhibition. *Cell.* 105:521–532. https://doi.org/10.1016/S0092-8674(01)00341-5

Garrido, J.J., P. Giraud, E. Carlier, F. Fernandes, A. Moussif, M.P. Fache, D. Debanne, and B. Dargent. 2003. A targeting motif involved in sodium channel clustering at the axonal initial segment. *Science.* 300:2091–2094. https://doi.org/10.1126/science.1085167

Gorbea, C., G.M. Goellner, K. Teter, R.K. Holmes, and M. Rechsteiner. 2004. Characterization of mammalian Ecm29, a 26 S proteasome-associated protein that localizes to the nucleus and membrane vesicles. *J. Biol. Chem.* 279:54849–54861. https://doi.org/10.1074/jbc.M410444200

Gorbea, C., G. Pratt, V. Ustrell, R. Bell, S. Sahasrabudhe, R.E. Hughes, and M. Rechsteiner. 2010. A protein interaction network for Ecm29 links the 26 S proteasome to molecular motors and endosomal components. *J. Biol. Chem.* 285:31616–31633. https://doi.org/10.1074/jbc.M110.154120

Grubb, M.S., and J. Burrone. 2010. Activity-dependent relocation of the axon initial segment fine-tunes neuronal excitability. *Nature.* 465:1070–1074. https://doi.org/10.1038/nature09160

Grubb, M.S., Y. Shu, H. Kuba, M.N. Rasband, V.C. Wimmer, and K.J. Bender. 2011. Short- and long-term plasticity at the axon initial segment. *J. Neurosci.* 31:16049–16055. https://doi.org/10.1523/JNEUROSCI.4064-11.2011

Gulledge, A.T., and J.J. Bravo. 2016. Neuron Morphology Influences Axon Initial Segment Plasticity. *eNeuro.* 3:ENEURO.0085-15.2016. https://doi.org/10.1523/ENEURO.0085-15.2016

Gulyás, A.I., A. Sík, J.A. Payne, K. Kaila, and T.F. Freund. 2001. The KCl cotransporter, KCC2, is highly expressed in the vicinity of excitatory synapses in the rat hippocampus. *Eur. J. Neurosci.* 13:2205–2217. https://doi.org/10.1046/j.0953-816x.2001.01600.x

Hedstrom, K.L., Y. Ogawa, and M.N. Rasband. 2008. AnkyrinG is required for maintenance of the axon initial segment and neuronal polarity. *J. Cell Biol.* 183:635–640. https://doi.org/10.1083/jcb.200806112

Hedstrom, K.L., X. Xu, Y. Ogawa, R. Frischknecht, C.I. Seidenbecher, P. Shrager, and M.N. Rasband. 2007. Neurofascin assembles a specialized extracellular matrix at the axon initial segment. *J. Cell Biol.* 178:875–886. https://doi.org/10.1083/jcb.200705119

Heubl, M., J. Zhang, J.C. Pressey, S. Al Awabdh, M. Renner, F. Gomez-Castro, I. Moutkine, E. Eugène, M. Russeau, K.T. Kahle, et al. 2017. $GABA_A$ receptor dependent synaptic inhibition rapidly tunes KCC2 activity via the Cl^--sensitive WNK1 kinase. *Nat. Commun.* 8:1776. https://doi.org/10.1038/s41467-017-01749-0

Hsu, M.T., C.L. Guo, A.Y. Liou, T.Y. Chang, M.C. Ng, B.I. Florea, H.S. Overkleeft, Y.L. Wu, J.C. Liao, and P.L. Cheng. 2015. Stage-Dependent Axon Transport of Proteasomes Contributes to Axon Development. *Dev. Cell.* 35:418–431. https://doi.org/10.1016/j.devcel.2015.10.018

Hsu, W.C., C.L. Nilsson, and F. Laezza. 2014. Role of the axonal initial segment in psychiatric disorders: function, dysfunction, and intervention. *Front. Psychiatry.* 5:109. https://doi.org/10.3389/fpsyt.2014.00109

Huang, C.Y., C. Zhang, T.S. Ho, J. Oses-Prieto, A.L. Burlingame, J. Lalonde, J.L. Noebels, C. Leterrier, and M.N. Rasband. 2017. αII Spectrin Forms a Periodic Cytoskeleton at the Axon Initial Segment and Is Required for Nervous System Function. *J. Neurosci.* 37:11311–11322. https://doi.org/10.1523/JNEUROSCI.2112-17.2017

Judson, M.C., M.L. Wallace, M.S. Sidorov, A.C. Burette, B. Gu, G.M. van Woerden, I.F. King, J.E. Han, M.J. Zylka, Y. Elgersma, et al. 2016. GABAergic Neuron-Specific Loss of Ube3a Causes Angelman Syndrome-Like EEG Abnormalities and Enhances Seizure Susceptibility. *Neuron.* 90:56–69. https://doi.org/10.1016/j.neuron.2016.02.040

Kahle, K.T., T.Z. Deeb, M. Puskarjov, L. Silayeva, B. Liang, K. Kaila, and S.J. Moss. 2013. Modulation of neuronal activity by phosphorylation of the K-Cl cotransporter KCC2. *Trends Neurosci.* 36:726–737. https://doi.org/10.1016/j.tins.2013.08.006

Kaila, K., T.J. Price, J.A. Payne, M. Puskarjov, and J. Voipio. 2014. Cation-chloride cotransporters in neuronal development, plasticity and disease. *Nat. Rev. Neurosci.* 15:637–654. https://doi.org/10.1038/nrn3819

Kajava, A.V., C. Gorbea, J. Ortega, M. Rechsteiner, and A.C. Steven. 2004. New HEAT-like repeat motifs in proteins regulating proteasome structure and function. *J. Struct. Biol.* 146:425–430. https://doi.org/10.1016/j.jsb.2004.01.013

Khazipov, R., I. Khalilov, R. Tyzio, E. Morozova, Y. Ben-Ari, and G.L. Holmes. 2004. Developmental changes in GABAergic actions and seizure susceptibility in the rat hippocampus. *Eur. J. Neurosci.* 19:590–600. https://doi.org/10.1111/j.0953-816X.2003.03152.x

Khirug, S., J. Yamada, R. Afzalov, J. Voipio, L. Khiroug, and K. Kaila. 2008. GABAergic depolarization of the axon initial segment in cortical principal neurons is caused by the Na-K-2Cl cotransporter NKCC1. *J. Neurosci.* 28:4635–4639. https://doi.org/10.1523/JNEUROSCI.0908-08.2008

Kole, M.H., and G.J. Stuart. 2012. Signal processing in the axon initial segment. *Neuron.* 73:235–247. https://doi.org/10.1016/j.neuron.2012.01.007

Lee, S.Y., A. De la Mota-Peynado, and J. Roelofs. 2011. Loss of Rpt5 protein interactions with the core particle and Nas2 protein causes the formation of faulty proteasomes that are inhibited by Ecm29 protein. *J. Biol. Chem.* 286:36641–36651. https://doi.org/10.1074/jbc.M111.280875

Leggett, D.S., J. Hanna, A. Borodovsky, B. Crosas, M. Schmidt, R.T. Baker, T. Walz, H. Ploegh, and D. Finley. 2002. Multiple associated proteins regulate proteasome structure and function. *Mol. Cell.* 10:495–507. https://doi.org/10.1016/S1097-2765(02)00638-X

Lehmann, A., A. Niewienda, K. Jechow, K. Janek, and C. Enenkel. 2010. Ecm29 fulfils quality control functions in proteasome assembly. *Mol. Cell.* 38:879–888. https://doi.org/10.1016/j.molcel.2010.06.016

Leonzino, M., M. Busnelli, F. Antonucci, C. Verderio, M. Mazzanti, and B. Chini. 2016. The Timing of the Excitatory-to-Inhibitory GABA Switch Is Regulated by the Oxytocin Receptor via KCC2. *Cell Reports.* 15:96–103. https://doi.org/10.1016/j.celrep.2016.03.013

Leterrier, C. 2018. The Axon Initial Segment: An Updated Viewpoint. *J. Neurosci.* 38:2135–2145. https://doi.org/10.1523/JNEUROSCI.1922-17.2018

Leterrier, C., J. Potier, G. Caillol, C. Debarnot, F. Rueda Boroni, and B. Dargent. 2015. Nanoscale Architecture of the Axon Initial Segment Reveals an Organized and Robust Scaffold. *Cell Reports.* 13:2781–2793. https://doi.org/10.1016/j.celrep.2015.11.051

Medina, I., P. Friedel, C. Rivera, K.T. Kahle, N. Kourdougli, P. Uvarov, and C. Pellegrino. 2014. Current view on the functional regulation of the neuronal K(+)-Cl(-) cotransporter KCC2. *Front. Cell. Neurosci.* 8:27. https://doi.org/10.3389/fncel.2014.00027

Mohler, P.J., A.O. Gramolini, and V. Bennett. 2002. The ankyrin-B C-terminal domain determines activity of ankyrin-B/G chimeras in rescue of abnormal inositol 1,4,5-trisphosphate and ryanodine receptor distribution in ankyrin-B (-/-) neonatal cardiomyocytes. *J. Biol. Chem.* 277:10599–10607. https://doi.org/10.1074/jbc.M110958200

Muir, J., and J.T. Kittler. 2014. Plasticity of GABAA receptor diffusion dynamics at the axon initial segment. *Front. Cell. Neurosci.* 8:151. https://doi.org/10.3389/fncel.2014.00151

Naydenov, A.V., E.A. Horne, C.S. Cheah, K. Swinney, K.L. Hsu, J.K. Cao, W. Marrs, J.L. Blankman, S. Tu, A.E. Cherry, et al. 2014. ABHD6 blockade exerts antiepileptic activity in PTZ-induced seizures and in spontaneous seizures in R6/2 mice. *Neuron.* 83:361–371. https://doi.org/10.1016/j.neuron.2014.06.030

Otero, M.G., M. Alloatti, L.E. Cromberg, A. Almenar-Queralt, S.E. Encalada, V.M. Pozo Devoto, L. Bruno, L.S. Goldstein, and T.L. Falzone. 2014. Fast axonal transport of the proteasome complex depends on membrane interaction and molecular motor function. *J. Cell Sci.* 127:1537–1549. https://doi.org/10.1242/jcs.140780

Panasenko, O.O., and M.A. Collart. 2011. Not4 E3 ligase contributes to proteasome assembly and functional integrity in part through Ecm29. *Mol. Cell. Biol.* 31:1610–1623. https://doi.org/10.1128/MCB.01210-10

Payne, J.A., T.J. Stevenson, and L.F. Donaldson. 1996. Molecular characterization of a putative K-Cl cotransporter in rat brain. A neuronal-specific isoform. *J. Biol. Chem.* 271:16245–16252. https://doi.org/10.1074/jbc.271.27.16245

Puskarjov, M., F. Ahmad, K. Kaila, and P. Blaesse. 2012. Activity-dependent cleavage of the K-Cl cotransporter KCC2 mediated by calcium-activated protease calpain. *J. Neurosci.* 32:11356–11364. https://doi.org/10.1523/JNEUROSCI.6265-11.2012

Rasband, M.N. 2010. The axon initial segment and the maintenance of neuronal polarity. *Nat. Rev. Neurosci.* 11:552–562. https://doi.org/10.1038/nrn2852

Rinetti-Vargas, G., K. Phamluong, D. Ron, and K.J. Bender. 2017. Periadolescent Maturation of GABAergic Hyperpolarization at the Axon Initial Segment. *Cell Reports.* 20:21–29. https://doi.org/10.1016/j.celrep.2017.06.030

Rivera, C., J. Voipio, J.A. Payne, E. Ruusuvuori, H. Lahtinen, K. Lamsa, U. Pirvola, M. Saarma, and K. Kaila. 1999. The K+/Cl- co-transporter KCC2 renders GABA hyperpolarizing during neuronal maturation. *Nature.* 397:251–255. https://doi.org/10.1038/16697

Rohrbough, J., and N.C. Spitzer. 1996. Regulation of intracellular Cl- levels by Na(+)-dependent Cl- cotransport distinguishes depolarizing from hyperpolarizing GABAA receptor-mediated responses in spinal neurons. *J. Neurosci.* 16:82–91. https://doi.org/10.1523/JNEUROSCI.16-01-00082.1996

Rossner, M., and K.M. Yamada. 2004. What's in a picture? The temptation of image manipulation. *J. Cell Biol.* 166(1):11–15. https://doi.org/10.1083/jcb.200406019

Russell, J.M. 2000. Sodium-potassium-chloride cotransport. *Physiol. Rev.* 80:211–276. https://doi.org/10.1152/physrev.2000.80.1.211

Schafer, D.P., S. Jha, F. Liu, T. Akella, L.D. McCullough, and M.N. Rasband. 2009. Disruption of the axon initial segment cytoskeleton is a new mechanism for neuronal injury. *J. Neurosci.* 29:13242–13254. https://doi.org/10.1523/JNEUROSCI.3376-09.2009

Sherman, D.L., S. Tait, S. Melrose, R. Johnson, B. Zonta, F.A. Court, W.B. Macklin, S. Meek, A.J. Smith, D.F. Cottrell, and P.J. Brophy. 2005. Neurofascins are required to establish axonal domains for saltatory conduction. *Neuron.* 48:737–742. https://doi.org/10.1016/j.neuron.2005.10.019

Smith, K.R., K.J. Kopeikina, J.M. Fawcett-Patel, K. Leaderbrand, R. Gao, B. Schürmann, K. Myczek, J. Radulovic, G.T. Swanson, and P. Penzes. 2014. Psychiatric risk factor ANK3/ankyrin-G nanodomains regulate the structure and function of glutamatergic synapses. *Neuron.* 84:399–415. https://doi.org/10.1016/j.neuron.2014.10.010

Swann, J.W., R.J. Brady, and D.L. Martin. 1989. Postnatal development of GABA-mediated synaptic inhibition in rat hippocampus. *Neuroscience.* 28:551–561. https://doi.org/10.1016/0306-4522(89)90004-3

Szabadics, J., C. Varga, G. Molnár, S. Oláh, P. Barzó, and G. Tamás. 2006. Excitatory effect of GABAergic axo-axonic cells in cortical microcircuits. *Science.* 311:233–235. https://doi.org/10.1126/science.1121325

Tai, H.C., H. Besche, A.L. Goldberg, and E.M. Schuman. 2010. Characterization of the Brain 26S Proteasome and its Interacting Proteins. *Front. Mol. Neurosci.* 3:12.

Terenzio, M., G. Schiavo, and M. Fainzilber. 2017. Compartmentalized Signaling in Neurons: From Cell Biology to Neuroscience. *Neuron.* 96:667–679. https://doi.org/10.1016/j.neuron.2017.10.015

Tseng, W.C., P.M. Jenkins, M. Tanaka, R. Mooney, and V. Bennett. 2015. Giant ankyrin-G stabilizes somatodendritic GABAergic synapses through opposing endocytosis of GABAA receptors. *Proc. Natl. Acad. Sci. USA.* 112:1214–1219. https://doi.org/10.1073/pnas.1417989112

Vacher, H., and J.S. Trimmer. 2012. Trafficking mechanisms underlying neuronal voltage-gated ion channel localization at the axon initial segment. *Epilepsia.* 53(Suppl 9):21–31. https://doi.org/10.1111/epi.12032

Verdoes, M., B.I. Florea, V. Menendez-Benito, C.J. Maynard, M.D. Witte, W.A. van der Linden, A.M. van den Nieuwendijk, T. Hofmann, C.R. Berkers, F.W. van Leeuwen, et al. 2006. A fluorescent broad-spectrum proteasome inhibitor for labeling proteasomes in vitro and in vivo. *Chem. Biol.* 13:1217–1226. https://doi.org/10.1016/j.chembiol.2006.09.013

Wang, F., X. Wang, L.A. Shapiro, M.L. Cotrina, W. Liu, E.W. Wang, S. Gu, W. Wang, X. He, M. Nedergaard, and J.H. Huang. 2017a. NKCC1 upregulation contributes to early post-traumatic seizures and increased post-traumatic seizure susceptibility. *Brain Struct. Funct.* 222:1543–1556. https://doi.org/10.1007/s00429-016-1292-z

Wang, X., I.E. Chemmama, C. Yu, A. Huszagh, Y. Xu, R. Viner, S.A. Block, P. Cimermancic, S.D. Rychnovsky, Y. Ye, et al. 2017b. The proteasome-interacting Ecm29 protein disassembles the 26S proteasome in response to oxidative stress. *J. Biol. Chem.* 292:16310–16320. https://doi.org/10.1074/jbc.M117.803619

Wani, P.S., A. Suppahia, X. Capalla, A. Ondracek, and J. Roelofs. 2016. Phosphorylation of the C-terminal tail of proteasome subunit α7 is required for binding of the proteasome quality control factor Ecm29. *Sci. Rep.* 6:27873. https://doi.org/10.1038/srep27873

Watanabe, M., and A. Fukuda. 2015. Development and regulation of chloride homeostasis in the central nervous system. *Front. Cell. Neurosci.* 9:371. https://doi.org/10.3389/fncel.2015.00371

Wefelmeyer, W., D. Cattaert, and J. Burrone. 2015. Activity-dependent mismatch between axo-axonic synapses and the axon initial segment controls neuronal output. *Proc. Natl. Acad. Sci. USA.* 112:9757–9762. https://doi.org/10.1073/pnas.1502902112

Wimmer, V.C., C.A. Reid, S. Mitchell, K.L. Richards, B.B. Scaf, B.T. Leaw, E.L. Hill, M. Royeck, M.T. Horstmann, B.A. Cromer, et al. 2010a. Axon initial segment dysfunction in a mouse model of genetic epilepsy with febrile seizures plus. *J. Clin. Invest.* 120:2661–2671. https://doi.org/10.1172/JCI42219

Wimmer, V.C., C.A. Reid, E.Y. So, S.F. Berkovic, and S. Petrou. 2010b. Axon initial segment dysfunction in epilepsy. *J. Physiol.* 588:1829–1840. https://doi.org/10.1113/jphysiol.2010.188417

Xu, K., G. Zhong, and X. Zhuang. 2013. Actin, spectrin, and associated proteins form a periodic cytoskeletal structure in axons. *Science.* 339:452–456. https://doi.org/10.1126/science.1232251

Yamada, J., A. Okabe, H. Toyoda, W. Kilb, H.J. Luhmann, and A. Fukuda. 2004. Cl- uptake promoting depolarizing GABA actions in immature rat neocortical neurones is mediated by NKCC1. *J. Physiol.* 557:829–841. https://doi.org/10.1113/jphysiol.2004.062471

Yang, Y., Y. Ogawa, K.L. Hedstrom, and M.N. Rasband. 2007. betaIV spectrin is recruited to axon initial segments and nodes of Ranvier by ankyrinG. *J. Cell Biol.* 176:509–519. https://doi.org/10.1083/jcb.200610128

Zhang, X., and V. Bennett. 1998. Restriction of 480/270-kD ankyrin G to axon proximal segments requires multiple ankyrin G-specific domains. *J. Cell Biol.* 142:1571–1581. https://doi.org/10.1083/jcb.142.6.1571

Zhang, X., J.Q. Davis, S. Carpenter, and V. Bennett. 1998. Structural requirements for association of neurofascin with ankyrin. *J. Biol. Chem.* 273:30785–30794. https://doi.org/10.1074/jbc.273.46.30785

Zhong, G., J. He, R. Zhou, D. Lorenzo, H.P. Babcock, V. Bennett, and X. Zhuang. 2014. Developmental mechanism of the periodic membrane skeleton in axons. *eLife.* 3:e04581. https://doi.org/10.7554/eLife.04581